

1 What caused record-breaking aerosol loading over the South China 2 Sea in April 2023

3 Saginela Ravindra Babu^{1*} and Neng-Huei Lin^{1,2*}

4 ¹Department of Atmospheric Sciences, National Central University, Taoyuan 32001, Taiwan.

5 ²Center for Environmental Monitoring and Technology, National Central University, Taoyuan
6 32001, Taiwan.

7 Correspondence to: S. Ravindra Babu (baburavindra595@gmail.com) and Neng-Huei Lin
8 (nhlin@cc.ncu.edu.tw).

9 Abstract:

10 In April 2023, record-breaking aerosol optical depth (AOD) levels were observed over the South
11 China Sea (SCS). This study investigates the sources, transport pathways, and large-scale
12 dynamical conditions associated with this extreme aerosol event. Observations from the Moderate
13 Resolution Imaging Spectroradiometer (MODIS) revealed the highest April AOD in the 2003-
14 2023 satellite record, with values increasing by approximately 150% relative to the 2003-2022
15 climatological mean and exceeding 4σ above normal conditions. Enhanced carbon monoxide (CO)
16 concentrations were simultaneously detected in the free to mid-troposphere (700-500 hPa) by
17 Measurements of Pollution in the Troposphere (MOPITT) and Atmospheric Infrared Sounder
18 (AIRS), indicating substantial long-range transport of combustion-related pollution. MODIS fire
19 count and burned-area datasets further indicated intensified biomass-burning (BB) activity over
20 northern Peninsular Southeast Asia (PSEA) during the same period. Backward trajectory
21 simulations using the NOAA Hybrid Single-Particle Lagrangian Integrated Trajectory (HYSPLIT)
22 model suggested that a large fraction of air masses arriving over the SCS originated from northern
23 PSEA, supporting the interpretation that BB emissions from this region contributed substantially
24 to the elevated aerosol loading over the SCS. Dynamical analyses revealed a persistent anti-
25 cyclonic anomaly over northern PSEA at 500 hPa, accompanied by an eastward-shifted Bay of
26 Bengal anticyclone at 700 hPa and a western North Pacific cyclonic anomaly at both levels. These
27 circulation anomalies likely altered the prevailing regional flow by shifting climatological
28 southerlies toward northerly anomalies, thereby favoring aerosol transport and accumulation over
29 the SCS. Overall, the results suggest that the extreme aerosol event was associated with the
30 combined influence of intensified BB emissions and anomalous atmospheric circulation,

31 highlighting the important role of coupled emissions and atmospheric dynamics in shaping
32 regional aerosol extremes.

33 ~~In April 2023, the South China Sea (SCS) experienced an unprecedented surge in aerosol loading,~~
34 ~~with aerosol optical depth (AOD) reaching the highest levels recorded during the 2-decade period~~
35 ~~of Moderate Resolution Imaging Spectroradiometer (MODIS) satellite data (2003–2023). AOD~~
36 ~~increased by ~150% relative to the long-term mean (2002–2022), indicating an anomaly exceeding~~
37 ~~4 σ , and was accompanied by pronounced enhancement in carbon monoxide (CO) at 700 and 500~~
38 ~~hPa. Using multi-sensor satellite measurements and MERRA-2 reanalysis, we investigated the~~
39 ~~sources, driving mechanisms, and atmospheric dynamics behind this extreme aerosol event.~~
40 ~~MODIS fire counts, burned-area data, and NOAA HYSPLIT back-trajectory analyses identify~~
41 ~~intense biomass burning (BB) across northern Peninsular Southeast Asia (PSEA) as the dominant~~
42 ~~source, particularly from Laos and Myanmar. The BB was facilitated by anomalous meteorological~~
43 ~~conditions associated with a persistent tropospheric anti-cyclonic anomaly over PSEA, which~~
44 ~~suppressed convection and promoted subsidence, elevated surface temperatures, and led to~~
45 ~~widespread drought. The dynamical large-scale circulation anomalies further revealed~~
46 ~~substantially altered transport pathways. A coupled dynamical pattern involving a western North~~
47 ~~Pacific (WNP) cyclone, a BoB anticyclone at 700 hPa, and a PSEA anticyclone at 500 hPa~~
48 ~~generated persistent northerly flow over the SCS, redirecting smoke plumes southward toward the~~
49 ~~SCS and southern BoB rather than along the climatological pathway toward Taiwan and the~~
50 ~~northwestern Pacific. These findings reveal how the combined influence of extreme BB emissions~~
51 ~~and anomalous circulation produced the record aerosol loading over the SCS, highlighting critical~~
52 ~~links among BB emissions and atmospheric dynamics in shaping regional air quality extremes.~~

53 **Key words: Aerosol loading; South China Sea; MODIS; ~~Biomass burning~~Biomass-burning**

54 **1. Introduction**

55 Atmospheric aerosols play a vital role in Earth's climate by impacting radiation balance, cloud
56 microphysics, and air quality (Ramanathan et al., 2001; Anderson et al., 2003; Forster et al., 2021;
57 IPCC, 2023). These particles scatter and absorb solar radiation directly, influencing radiative
58 effects, and also modify cloud properties, lifespan, and precipitation by serving as nuclei for
59 condensation and ice formation. As a result, aerosols affect atmospheric thermodynamics, cloud–
60 radiation interactions, and the water cycle (Twomey et al., 1977; IPCC, 2023). Monitoring aerosol

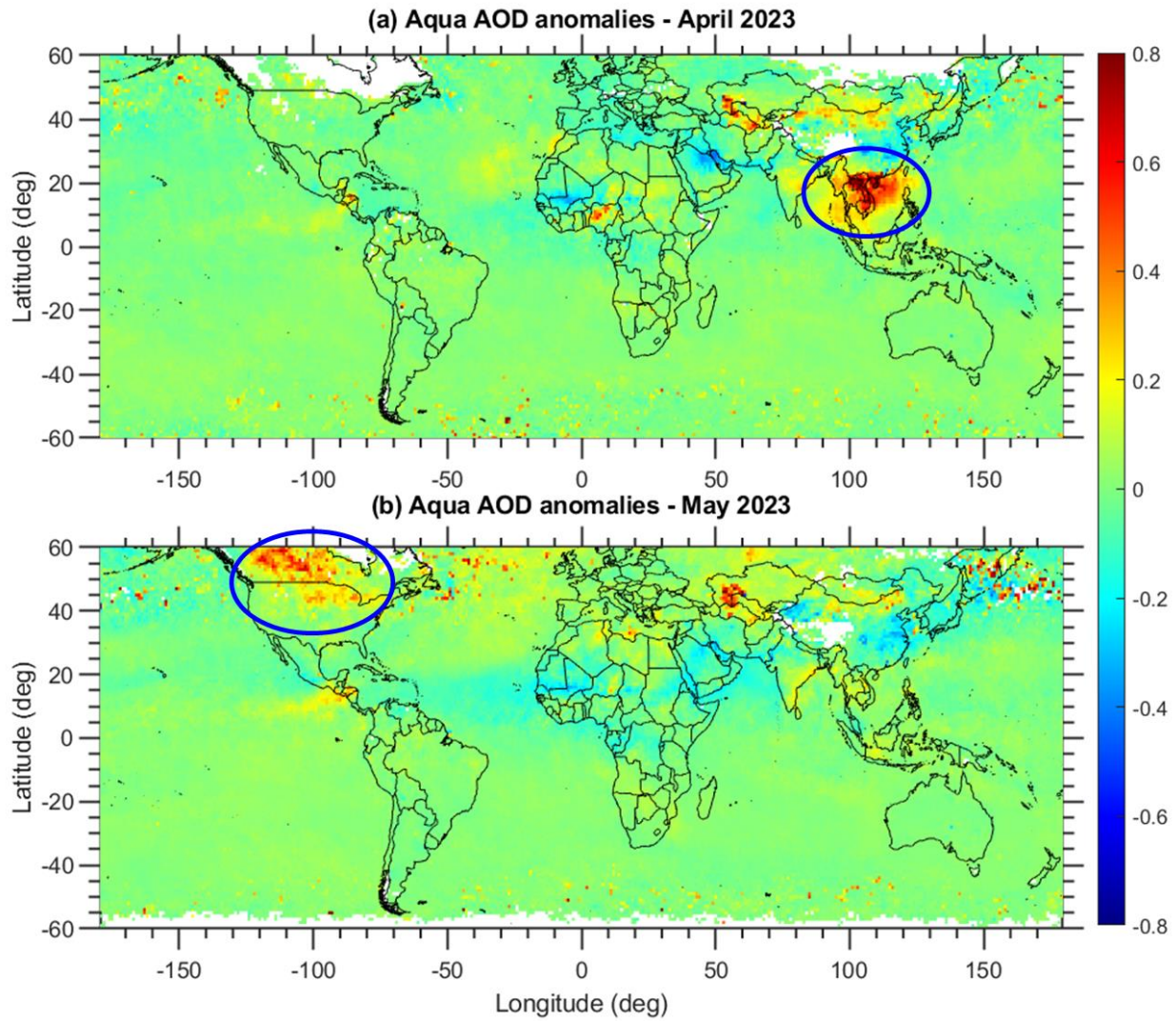
61 levels over remote ocean regions is especially important because these areas provide a baseline for
62 natural background aerosol levels and help evaluate the effects of long-range transport on regional
63 climate through radiative and cloud processes (Pani et al., 2023). In addition to anthropogenic
64 emissions, natural events such as wildfires and agricultural biomass-burning (BB) are significant
65 episodic sources, emitting large quantities of aerosol particles and trace gases that substantially
66 affect both regional and global climate systems (Crutzen and Andreae, 1990; Ramanathan et al.,
67 2001; Lin et al., 2013; Reid et al., 2013; Kolden et al., 2024).

68 The South China Sea (SCS), situated in Asia, is the largest marginal sea in the tropical–
69 subtropical western North Pacific (WNP), serving as a vital natural laboratory for examining
70 aerosol variability in a relatively pristine marine environment (Reid et al., 2013; Lin et al., 2013;
71 Pani et al., 2023). Although it is an oceanic region, the atmosphere over the SCS is significantly
72 influenced by emissions from nearby continents and regional circulation patterns (Pani et al.,
73 2023). Typically, the SCS is dominated by a monsoon system, with the northeast monsoon
74 occurring during boreal winter and spring, and the southwest monsoon during boreal summer and
75 autumn (Cui et al., 2016). These seasonal wind patterns play a key role in aerosol transport, often
76 carrying natural and human-made pollutants from East Asia into the SCS basin over long distances.
77 In addition to continental outflow from East Asia, ~~biomass-burning~~BB emissions from
78 surrounding areas notably influence aerosol concentrations over the SCS. During the summer
79 monsoon months, particularly August to October, persistent peatland and forest fires across the
80 Maritime Continent (MC) generate large smoke plumes that drift toward the southern SCS
81 (Ravindra Babu et al., 2023). Moreover, extensive open ~~BB~~biomass-burning in spring over
82 Peninsular Southeast Asia (PSEA), including Myanmar, Thailand, Cambodia, Laos, and Vietnam,
83 serves as a key source of aerosols affecting the SCS atmosphere (Chan et al., 2003; Ou-Yang et
84 al., 2012; Yadav et al., 2017; Liao et al., 2021; Wang et al., 2021; Pani et al., 2023; Wang et al.,
85 2025). This region is recognized as a global hotspot for ~~BB~~biomass-burning (Lin et al., 2013; Reid
86 et al., 2013; Cohen, 2014; Cohen et al., 2017; Pani et al., 2019), significantly contributing to carbon
87 emissions and aerosol loading during the peak fire season in March and April (Ravindra Babu and
88 Lin, 2023). These fires mainly stem from slash-and-burn farming practices occurring annually
89 across PSEA (Lee et al., 2016; Tsay et al., 2016; Huang et al., 2020), releasing substantial
90 particulate matter and trace gases into the air (Ou-Yang et al., 2022). As a result, aerosol variability
91 in the SCS region is largely driven by the interaction between regional emission sources and the

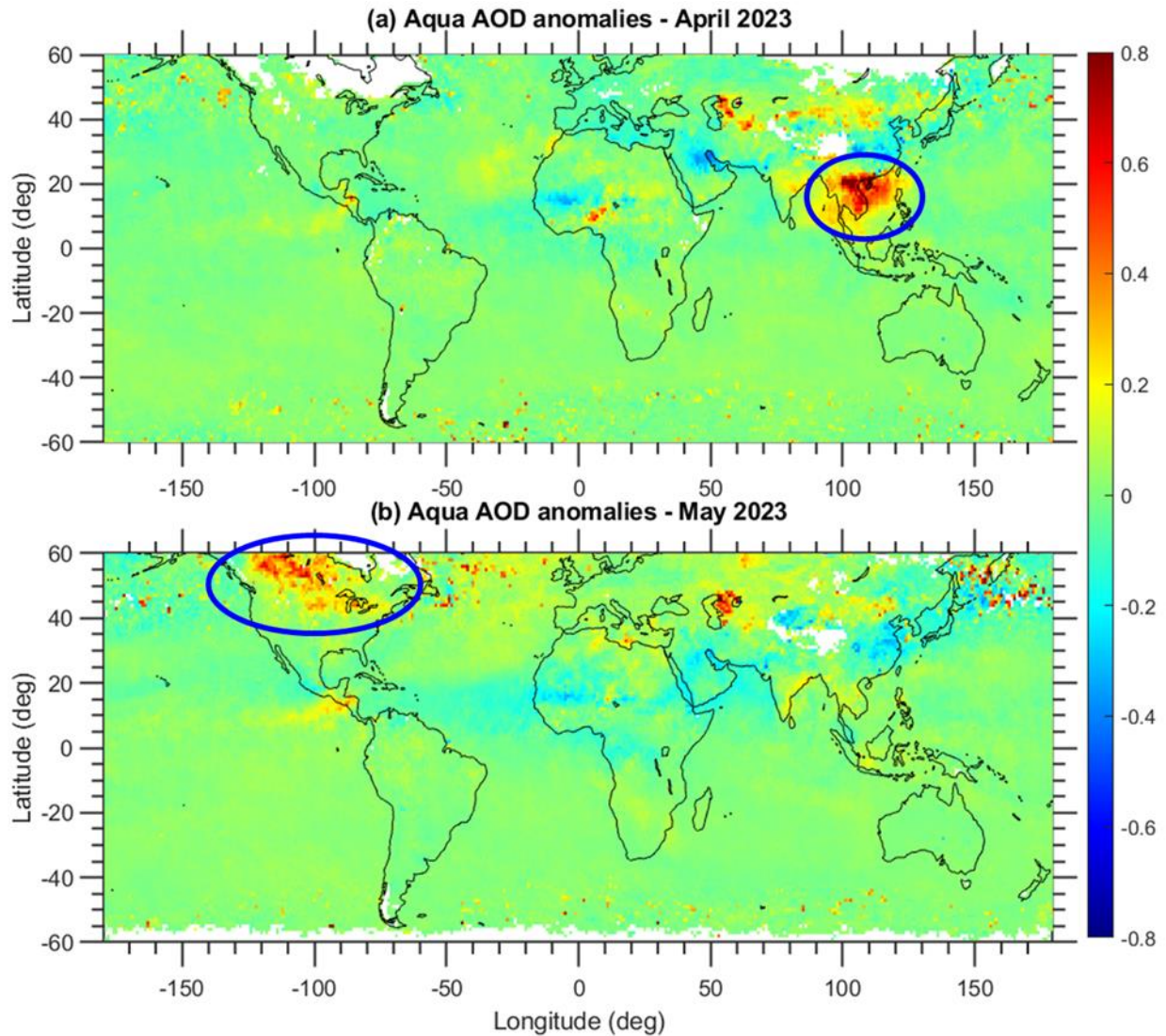
92 prevailing monsoon circulation, which influences aerosol transport, dispersion, and accumulation
93 within the basin (Pani et al., 2023).

94 The year 2023 saw exceptional wildfires worldwide due to record-high global mean surface
95 temperatures, which affected carbon emissions and aerosol levels (Esper et al., 2024; Forster et al.,
96 2024; Min, 2024; Raghuraman et al., 2024; Kolden et al., 2024; Liu et al., 2024; Byrne et al., 2024;
97 MacCarthy et al., 2024). It is reported that 70% of the total burning occurs in the Northern
98 Hemisphere (Kolden et al., 2024). Among all, Canadian wildfires emerged as the primary hotspot,
99 with significant fires in both the eastern and western regions causing notable increases in carbon
100 monoxide (CO) and tropospheric aerosols over the past twenty years (Liu et al., 2024; Byrne et
101 al., 2024; MacCarthy et al., 2024). Although the unprecedented Canadian wildfires in 2023
102 received considerable scientific attention and were well documented in several studies, the record-
103 breaking aerosol loading over the SCS in April 2023 attracted relatively little international
104 attention. The historic event over the SCS in April 2023 can be seen through the Moderate
105 Resolution Imaging Spectroradiometer (MODIS) Aqua AOD anomalies compared to the long-
106 term mean (2003-2022), which shows extreme positive anomalies over the SCS and surrounding
107 regions during that month, contrasting with the rest of the globe (**Fig. 1**). However, AOD
108 anomalies in May illustrate the absence of positive anomalies over the SCS and instead show
109 higher positive anomalies over North America, which are related to the Canadian wildfires. The
110 time series of monthly mean AOD over the SCS further confirms a record-high AOD in April 2023
111 relative to the MODIS data from 2003 to 2023 (**Fig. 2d**). The exceptional aerosol loading in April
112 2023 is unusual for remote marine locations such as the SCS and warrants further investigation.
113 In this study, we investigated the factors and physical processes that contributed to the
114 unprecedented aerosol levels observed in April 2023, using extensive data collected from multiple
115 sources over an extended period. The following three major topics are examined in detail within
116 this study:

- 117 • How extreme are these AOD anomalies, and what magnitude was increased?
- 118 • What are the sources for these record-breaking aerosol loadings over SCS?
- 119 • Were dynamic and large-scale circulations responsible for this event?



120



121

122 **Figure 1.** MODIS Aqua measured AOD anomalies in (a) April 2023 and (b) May 2023 compared
 123 to the long-term mean (2003-2022). The highlighted circles in (a) and (b) indicate the AOD
 124 anomalies over the South China Sea (SCS) and Canada regions. This figure highlights that the
 125 AOD anomalies observed by MODIS are significant and particularly pronounced over the SCS
 126 compared to the other areas globally. It illustrates the unique characteristics of April 2023
 127 compared to long-term mean. Data visualizations produced using MATLAB 2023b
 128 (<https://matlab.mathworks.com>).

129 **2. Data and Methodology**

130 **2.1 Data**

131 This study relies entirely on publicly available data, covering the period from 2003 to 2023. We
 132 used data products from various satellite measurements, ground-based observations, and reanalysis
 133 products.

134 **2.1.1 Satellite remote sensing measurements**

135 **Moderate Resolution Imaging Spectroradiometer (MODIS)**

136 MODIS is a passive sensor aboard the Aqua and Terra satellites, which are in [sun-synchronous](#)
137 [orbits and cross a sun-synchronous orbit, and pass](#) the Equator in the morning (Aqua) and afternoon
138 (Terra). From MODIS satellite measurements, we utilized aerosol optical depth (AOD), fire
139 counts, fire radiative power (FRP), cloud fraction, and burned area products. We used Level 3
140 monthly AOD at $1^\circ \times 1^\circ$ spatial resolution derived from the mean of the Dark Target and Deep
141 Blue Combined Aerosol Products from the Terra satellite (MOD08_M3 Collection 6.1) and Aqua
142 satellite (MYD08_M3 Collection 6.1) (Platnick et al., 2015; Buchholz et al., 2020). For MODIS
143 AOD, the estimated uncertainty is approximately ± 0.05 over ocean and ± 0.15 over land. The
144 Collection 6.1 (C6.1) products used in this study have been shown to capture temporal variations
145 effectively and agree closely with ground-based observations (Wei et al., 2019a). Validation
146 against AERosol RObotic NETwork (AERONET) measurements demonstrates that the merged
147 Dark Target and Deep Blue (DTB) products accurately capture aerosol variability at both regional
148 and global scales (Sayer et al., 2014; Wei et al., 2019b). Additionally, we used MODIS's daily fire
149 counts and fire radiative power (FRP) products (Giglio et al., 2006, 2016, 2018). Direct fire counts
150 from MODIS were obtained from the Fire Information for Resource Management System
151 (FIRMS) dataset. We selected all MODIS fire counts from the Terra and Aqua sensors with a
152 confidence level of at least 80%. Finally, we utilized Cloud Fraction data from both the Terra and Aqua
153 satellites.

154 **Measurements Of Pollution In The Troposphere (MOPITT)**

155 MOPITT is a multi-channel thermal infrared (TIR) and near-infrared (NIR) instrument operating
156 on board the sun-synchronous polar-orbiting NASA Terra satellite. This study uses a version 9
157 (MOP03TM_9) gridded monthly product (Worden et al., 2010; Deeter et al., 2019). For more
158 details on the retrieval algorithm, validation, and uncertainties in MOPITT CO, see Deeter et al.
159 (2019).

160 **Atmospheric Infrared Sounder (AIRS)**

161 In addition to the MOPITT measurements, we used CO from the AIRS instrument on the NASA
162 Aqua satellite, which provides CO at multiple vertical levels twice daily and has near-global

163 coverage. AIRS uses wavenumbers 2183–2200 cm⁻¹ (4.58–4.5 μm) for retrieving CO (McMillan
164 et al., 2005). The V9 level 3 CO product, available at 1° × 1° resolution at 700 and 500 hPa levels,
165 was utilized in the present study. AIRS sensitivity to CO is broad and optimal in the mid-
166 troposphere between approximately 300 and 600 hPa (Warner et al., 2007, 2013; AIRS project,
167 2019). CO retrievals exhibit a 6%–10 % bias between 900 and 300 hPa with a root mean square
168 error of 8%–12 % (McMillan et al., 2011). In addition to CO, we also utilized ~~ozone~~, surface
169 temperature, and outgoing longwave radiation (OLR) data from the AIRS satellite.

170 **Global Precipitation Climatology Project (GPCP)**

171 The Global Precipitation Climatology Project (GPCP) Version 3.2 Satellite-Gauge (SG)
172 Combined Precipitation Data Set was used during the study period. The data is available for
173 download from <https://measures.gesdisc.eosdis.nasa.gov/data/GPCP/GPCPMON.3.2/> (last
174 accessed June 5, 2025).

175 **Cloud-Aerosol LIDAR with Orthogonal Polarization (CALIOP)**

176 The CALIOP sensor on the Cloud-Aerosol Lidar and Infrared Pathfinder Satellite Observations
177 (CALIPSO) satellite provides data on atmospheric aerosols, including aerosol layer heights and
178 thicknesses, optical depth, aerosol type, and other optical properties (Omar et al., 2009; Kim et al.,
179 2018). In our study, we used vertical aerosol-type images available on the CALIPSO website.

180 **2.1.2 Reanalysis/model products**

181 **MERRA-2 reanalysis**

182 We used monthly mean geopotential height, wind vectors (zonal and meridional wind speeds),
183 and, total column black carbon, organic carbon, and particulate matter from the Modern-Era
184 Retrospective Analysis for Research and Applications, version 2 (MERRA-2). MERRA-2 is the
185 latest atmospheric reanalysis data produced by the NASA Global Modeling and Assimilation
186 Office (GMAO; Gelaro et al., 2017). The horizontal resolution of the MERRA-2 reanalysis is 0.5°
187 × 0.625°.

188 **Global Land Data Assimilation System (GLDAS)**

189 Monthly mean soil moisture content (10 - 40 cm underground) from the Global Land Data
190 Assimilation System (GLDAS)_NOAH025_M v2.1 is utilized. The data can be downloaded from

191 https://hydro1.gesdisc.eosdis.nasa.gov/data/GLDAS/GLDAS_NOAH025_M.2.1/ (last accessed:
192 June 05, 2025).

193 **2.1.3 Ground-based observations**

194 **AERONET**

195 In this study, we use the latest version (V3) of Level 2.0 AERONET data from two stations:
196 Dongsha Island (also called the Pratas Islands; Dongsha_Island, 20.70°N, 116.73°E, 5 m above
197 sea level) and Lulin Atmospheric Background Station (LABS, 23°28'N, 120°52'E, 2,862 m; Sheu
198 et al., 2010). These offer cloud-screened, quality-checked direct-sun AOD retrievals with
199 uncertainties of about ± 0.01 in the visible and ± 0.02 in the ultraviolet range (Giles et al., 2019;
200 Sinyuk et al., 2020).

201 The summary of the major data used in the present study is presented in **Table 1**.

202 **Table 1.** Details of various data products used in the present study.

Data	Resolution	Source
Aerosol Optical Depth (AOD)	$1^\circ \times 1^\circ$	Aqua and Terra satellite/MODIS
Carbon Monoxide (CO)	$1^\circ \times 1^\circ$	MOPITT and AIRS
Burned Area (BA)	500 m	Aqua and Terra satellite/MODIS
MODIS Collection 6.1 Fire Anomalies		combined Terra and Aqua satellite/MODIS
Wind and Geopotential Height	$0.5^\circ \times 0.625^\circ$	MERRA reanalysis

203

204 **2.2 Methodology**

205 The anomalies in the various parameters for April 2023 were estimated by subtracting the April
206 background long-term mean (2003-2022) from April 2023 value.

207 The magnitude of the AOD/CO enhancement in April 2023 above the long-term background was
208 determined by comparing the average of April 2003-2022. We obtained the percentage change in
209 AOD/CO relative to the respective background using Equation 1:

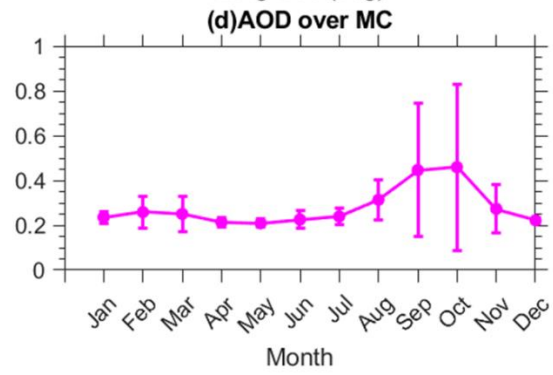
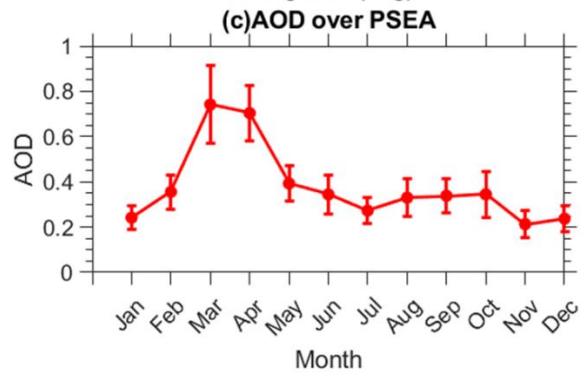
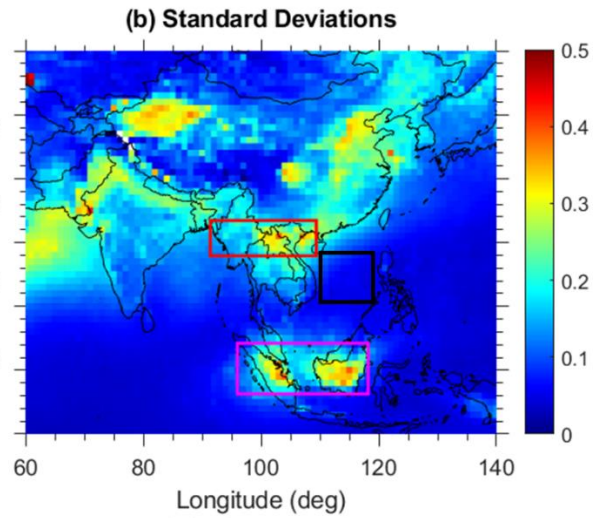
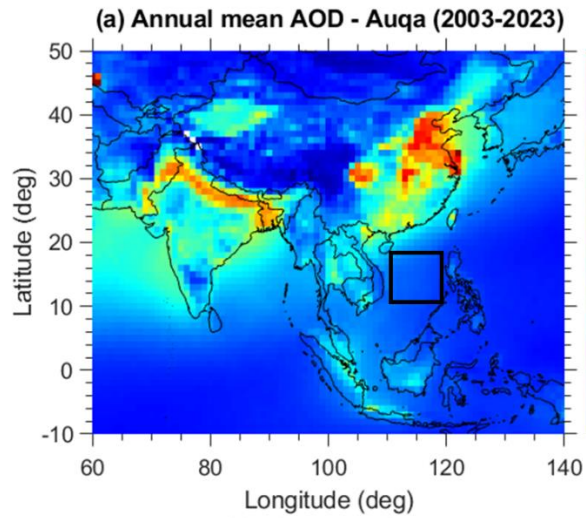
$$210 \quad \text{Relative change in percentage} = \left(\frac{x_i - \bar{x}}{\bar{x}} \right) \times 100 \quad (\text{Eq. 1})$$

211 where x_i represents the monthly mean of April in 2023, and \bar{x} is the long-term mean of April
212 calculated using the data from 2003 to 2022.

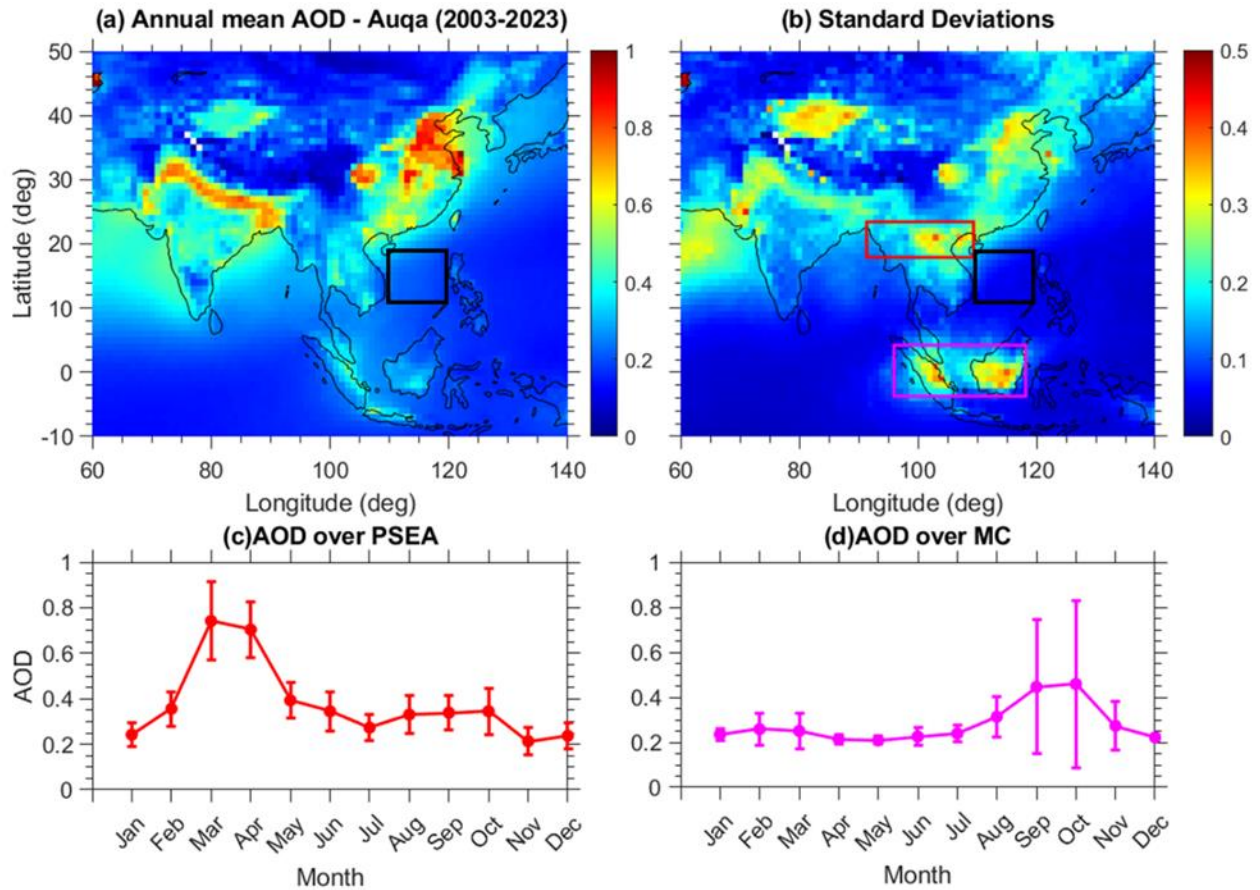
213 **3. Results and Discussion**

214 **3.1 Record-breaking aerosol loading over SCS in April 2023**

215 Aerosol optical depth (AOD) is a common metric for measuring atmospheric aerosol loading and
216 is crucial for radiative forcing assessments (Hirsch and Koren, 2021). In this study, we use AOD
217 data from the MODIS instruments aboard the Aqua and Terra satellites for the period. Before
218 analyzing the unusual AOD conditions observed in April 2023, we first characterize the long-term
219 AOD behavior over the study area using two decades of MODIS data. The spatial patterns of the
220 long-term annual mean AOD and its associated standard deviation across the Asian region are
221 shown in **Figures 2a** and **2b**, respectively. Additionally, the long-term monthly-mean variability
222 of AOD over the two main **biomass-burning (BB)** regions surrounding the SCS, namely PSEA and
223 the MC, is shown in **Figures 2c** and **2d**. The relatively low AOD levels and small standard
224 deviations over the SCS suggest the dominance of a relatively clean marine environment. The
225 seasonal cycle of AOD shows clear peaks linked to regional BB activities (**Figs. 2c** and **2d**). Over
226 PSEA, AOD peaks during March–April, while over the MC, the peak occurs in September–
227 October. These seasonal maxima align with well-known BB activity periods in these areas
228 (Ravindra Babu and Lin, 2024; Chang et al., 2024). The fire season over the MC usually runs from
229 August to October, whereas PSEA experiences intense BB activity from January to April, with a
230 notable peak in March.

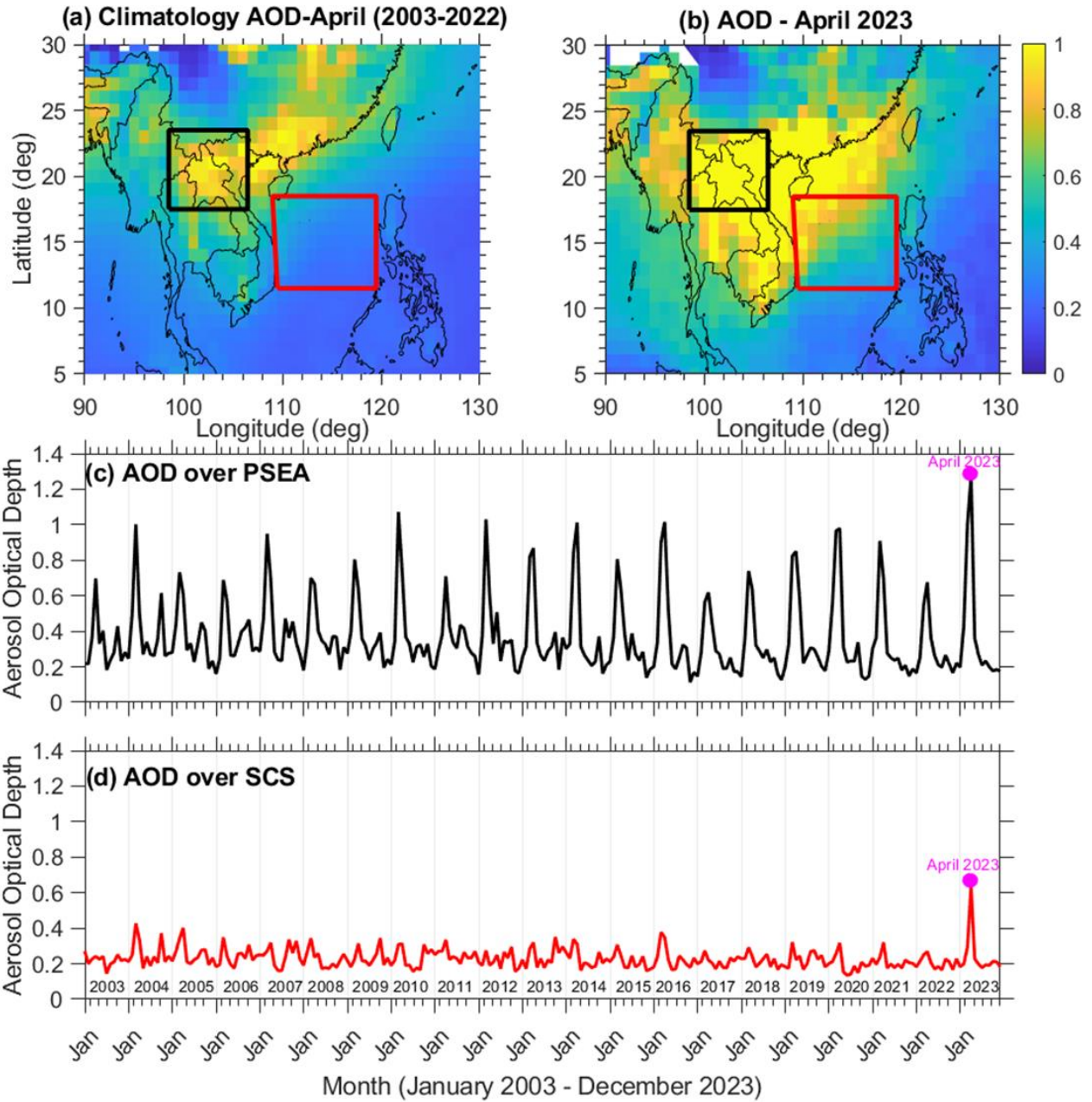


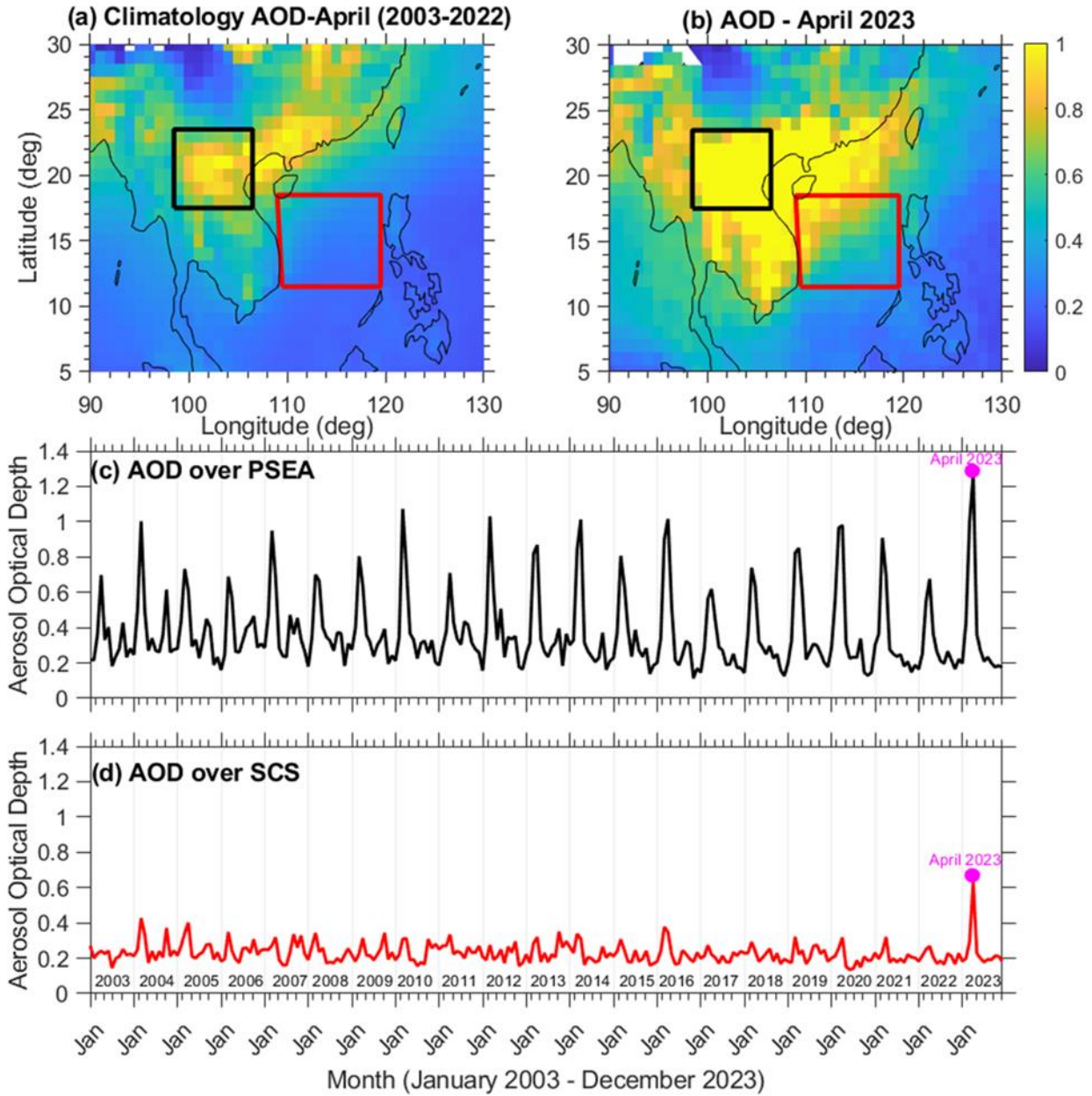
231



232

233 **Figure 2.** Climatological mean distribution of MODIS (a) Aerosol Optical Depth (AOD) and (b)
 234 respective standard deviations. The black box illustrated in both figures emphasizes the specific
 235 area of the South China Sea (SCS) that is the primary focus of this research. (11-18°N,109-119°E).
 236 The red and magenta boxes indicate the PSEA and MC, two significant biomass-burning regions
 237 near the SCS. The long-term average seasonal variation in AOD is illustrated over (c) PSEA and
 238 (d) MC.



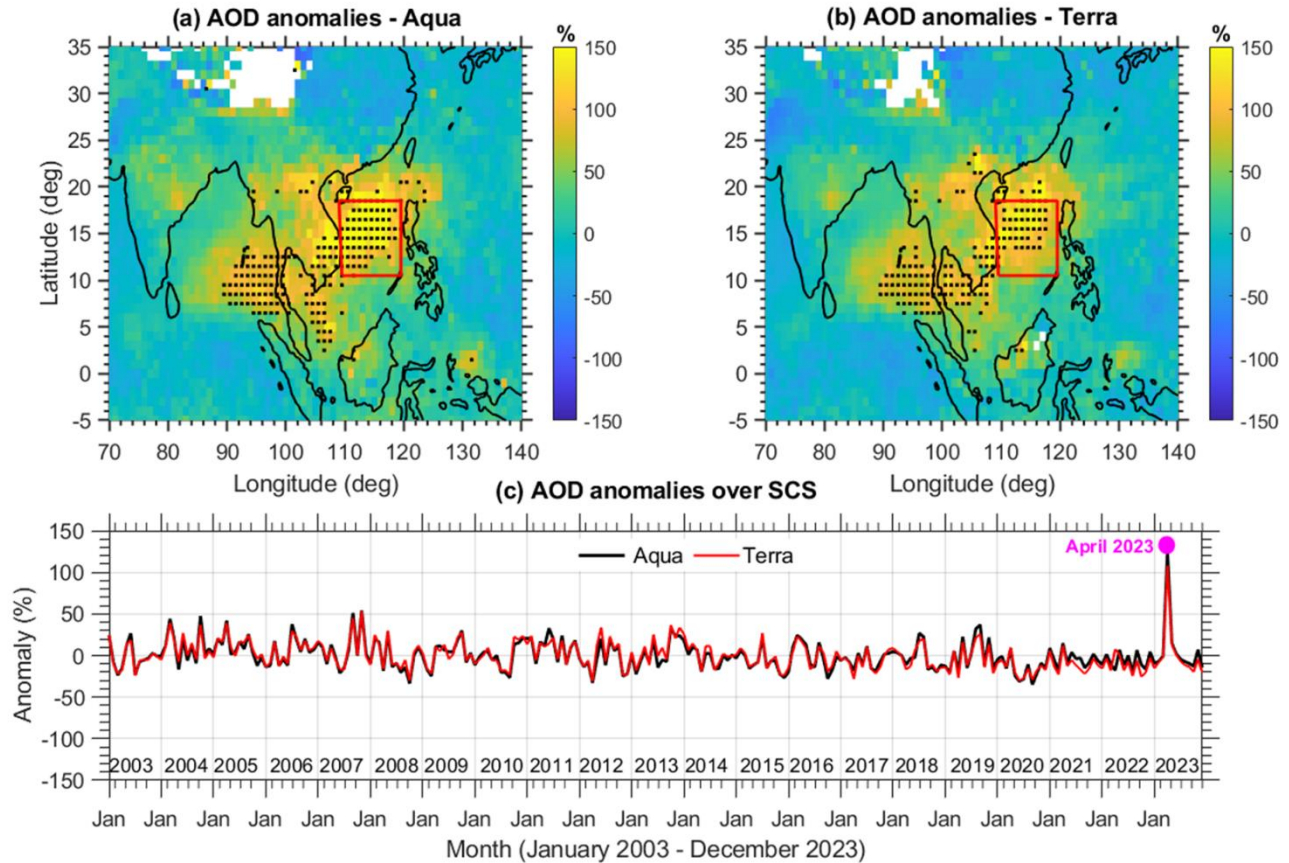


240

241 **Figure 3.** Spatial distribution of (a) Inter-annual (2003 to 2022) monthly average AOD values for
 242 April. (b) Monthly AOD values for April 2023. A notable increase in AOD values is observed
 243 over the Peninsular Southeast Asia (PSEA) and the South China Sea (SCS). AOD distribution
 244 averaged in April over the past two decades showed a belt of high aerosol loading extending from
 245 northern Laos to the southern coast of China. During April 2023, extreme AOD values were
 246 observed across the entire PSEA, extending to coastal South China and the SCS. (c) Time series
 247 of average monthly mean AOD values over the northern PSEA (17-23°N, 99- 106°E), and (d) over
 248 the SCS (11-18°N,109-119°E) from January 2003 to December 2023. The magenta dot in subplots
 249 (c) and (d) marks the AOD values during April 2023.

250 To emphasize the anomalous conditions in April 2023, we present the spatial distribution of April
251 AOD over the study region for both the long-term average and April 2023. The long-term average
252 April AOD for 2003–2022 and the corresponding April 2023 AOD distribution are shown in
253 **Figures 3a** and **3b**. Moreover, the time series of monthly mean AOD from 2003 to 2023 over
254 northern PSEA (17–23°N, 99–106°E) and the SCS (11–18°N, 109–119°E) are displayed in
255 **Figures 3c** and **3d**. The AOD distribution in April over two decades indicates high aerosol loading
256 from northern Laos to coastal South China (15–25°N, 100–120°E). In April 2023, extreme AOD
257 values extended from PSEA to South China and SCS, with the highest values centered between
258 northern Laos and the SCS. Record-breaking AOD levels were observed for the area averaged
259 over the SCS in April 2023, showing a nominal increase in northern PSEA (**Fig. 3c**). However,
260 the highest AOD value for northern PSEA in April 2023 correlates with record AOD over the SCS.
261 Long-term monthly mean AOD from Aqua and Terra (2003–2023) exhibited a strong correlation
262 of 0.97, confirming the consistency and reliability of these observations (**Fig. S1a** in the
263 Supplement). To assess the magnitude of the increase, we estimated the percentage change in AOD
264 by comparing April 2023 with the long-term April average from 2003 to 2022.

265



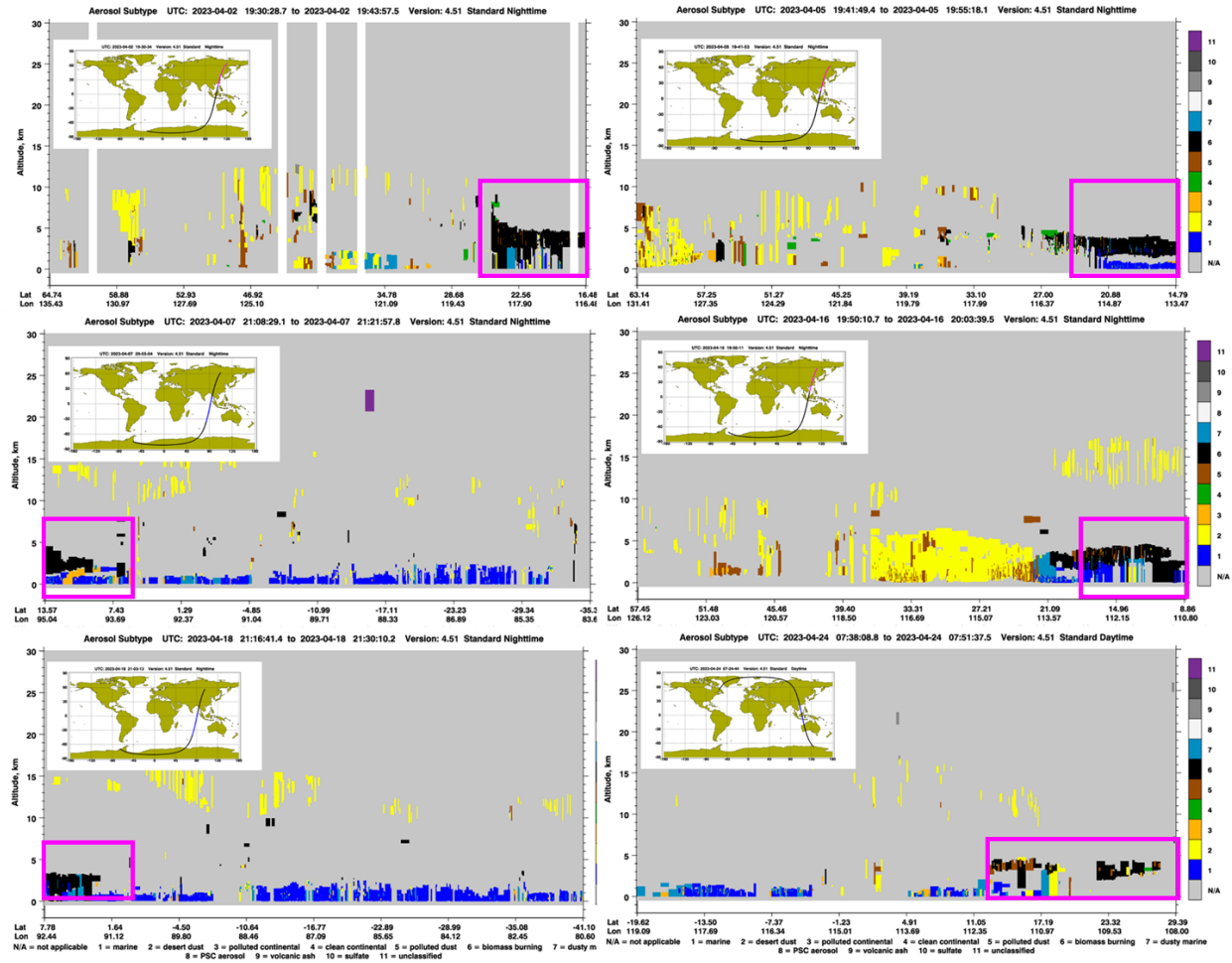
266

267 **Figure 4.** Spatial distribution of the change (%) in Aerosol Optical Depth (AOD) values during
 268 April 2023 compared with the inter-annual April average (2003-2022). (a) AOD anomalies are
 269 obtained from the MODIS Aqua and (b) from the MODIS Terra satellite. The black dots indicate
 270 that the anomalies exceed 4σ of the long-term mean. (c) Time series of area-averaged AOD
 271 anomalies expressed in percentage change over the South China Sea (SCS) domain from the Aqua
 272 (black line) and Terra (red line) satellites. The most pronounced enhancement occurred over the
 273 SCS, where April AOD anomalies exceeded 4σ above the long-term mean.

274 **Figures 4a and 4b** illustrate the spatial extent of AOD anomalies, shown as percentage
 275 changes, based on data from MODIS Aqua and Terra satellites. In April 2023, there was a
 276 widespread and unexpected increase of about 150% across most of the SCS and southern Bay of
 277 Bengal (BoB), with anomalies surpassing roughly 4 standard deviations. The area-averaged AOD
 278 anomalies (%) over the SCS, indicated by the black line for Aqua and the red line for Terra, reveal
 279 that the April 2023 peak was the highest on record compared to data from 2003 to 2023,
 280 emphasizing the extreme AOD intensity that month. These satellite observations were also
 281 supported by ground-based measurements from AERONET. The only operational AERONET
 282 remote station downwind of PSEA ~~BB~~biomass-burning, with over a decade of continuous AOD

283 measurements (**Fig. S2a** in the Supplement), within the SCS region is located on Dongsha Island
284 (also known as Pratas Island, 20.70°N, 116.73°E; 5 m a.s.l.). Analysis of monthly mean AOD data
285 from Dongsha Island indicates that April 2023 had the highest AOD value during the observational
286 period from January 2009 to December 2023 (**Fig. S2c** in the Supplement). AERONET
287 comparisons show strong correlations with MODIS AOD: 0.86 for Aqua and 0.87 for Terra (**Fig.**
288 **S3** in the Supplement), supporting the reliability of the satellite observations. Because AOD is a
289 column-integrated measure, it does not provide information on the vertical distribution of aerosols.
290 To address this limitation, we further analyzed vertical distribution images of aerosols from the
291 Cloud-Aerosol Lidar and Infrared Pathfinder Satellite Observation (CALIPSO), which reveal
292 pronounced enhancements in smoke aerosol over the SCS (**Fig. 5**). Elevated smoke layers were
293 also observed over the southern BoB in April 2023, predominantly within the mid-troposphere at
294 altitudes of approximately 2-5 km. Consistent with these CALIPSO lidar observations, MERRA-
295 2 reanalysis data indicate substantial increases in aerosol mass concentrations in 2023, with black
296 carbon (BC) increasing by ~250% and organic carbon (OC) by ~350% (**Fig. S4** in the Supplement).
297 The most pronounced enhancements occur between 700 and 600 hPa, closely matching the altitude
298 range identified by CALIPSO. The concurrence of satellite (MODIS and CALIPSO) and
299 reanalysis data points to a severe pollution episode in April 2023 over and surrounding regions of
300 the SCS, characterized by an elevated aerosol layer indicative of long-range-transported ~~biomass-~~
301 ~~burning~~BB smoke. Notably, the SCS is a relatively clean remote marine region with limited local
302 aerosol sources. In such environments, enhanced aerosol loading is typically associated with long-
303 range transport of pollutants from surrounding continental regions (Pani, 2023). Given the
304 potential influence of long-range pollution transport, we further analyzed variations in carbon
305 monoxide (CO), a widely used tracer of ~~biomass-burning~~BB emissions due to its relatively long
306 atmospheric lifetime (~1–2 months) and strong association with incomplete combustion (Ravindra
307 Babu et al., 2023). We investigated CO changes across the study region using measurements from
308 the MOPITT and AIRS satellites, which together provide more than two decades of continuous
309 CO observations. CO data at 700 and 500 hPa from both satellites were analyzed for the period
310 2003–2023, with the 500 hPa level representing the altitude of maximum sensitivity for CO
311 retrievals (Buchholz et al., 2021).

312

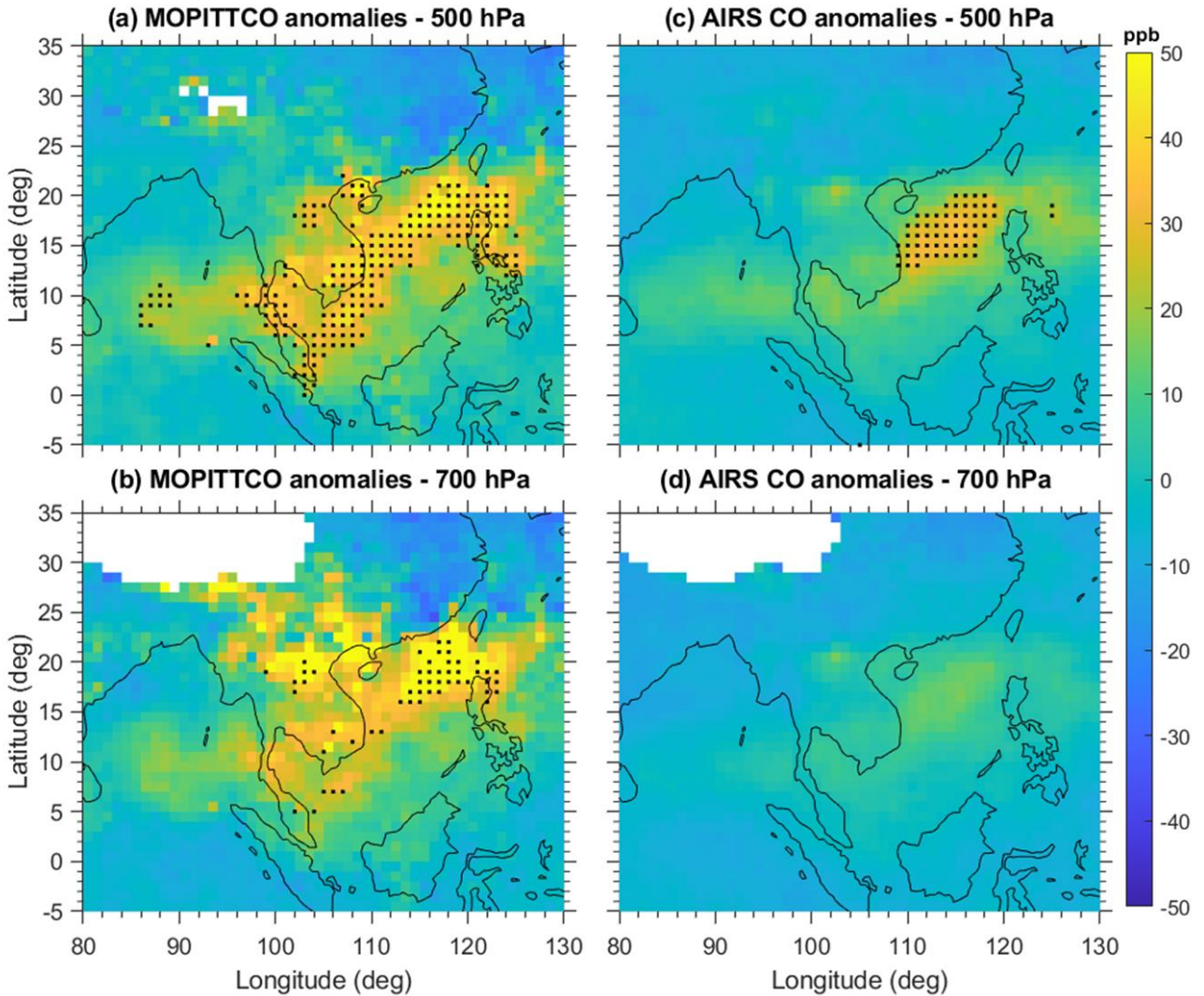


313

314 **Figure 5.** Aerosol subtype images obtained by the CALIPSO observations during various days in
 315 April 2023. The highlighted magenta box indicates elevated smoke over the [South China Sea](#)
 316 ([SCS](#)) and the southern Bay of Bengal. Smoke aerosol is shown in black.

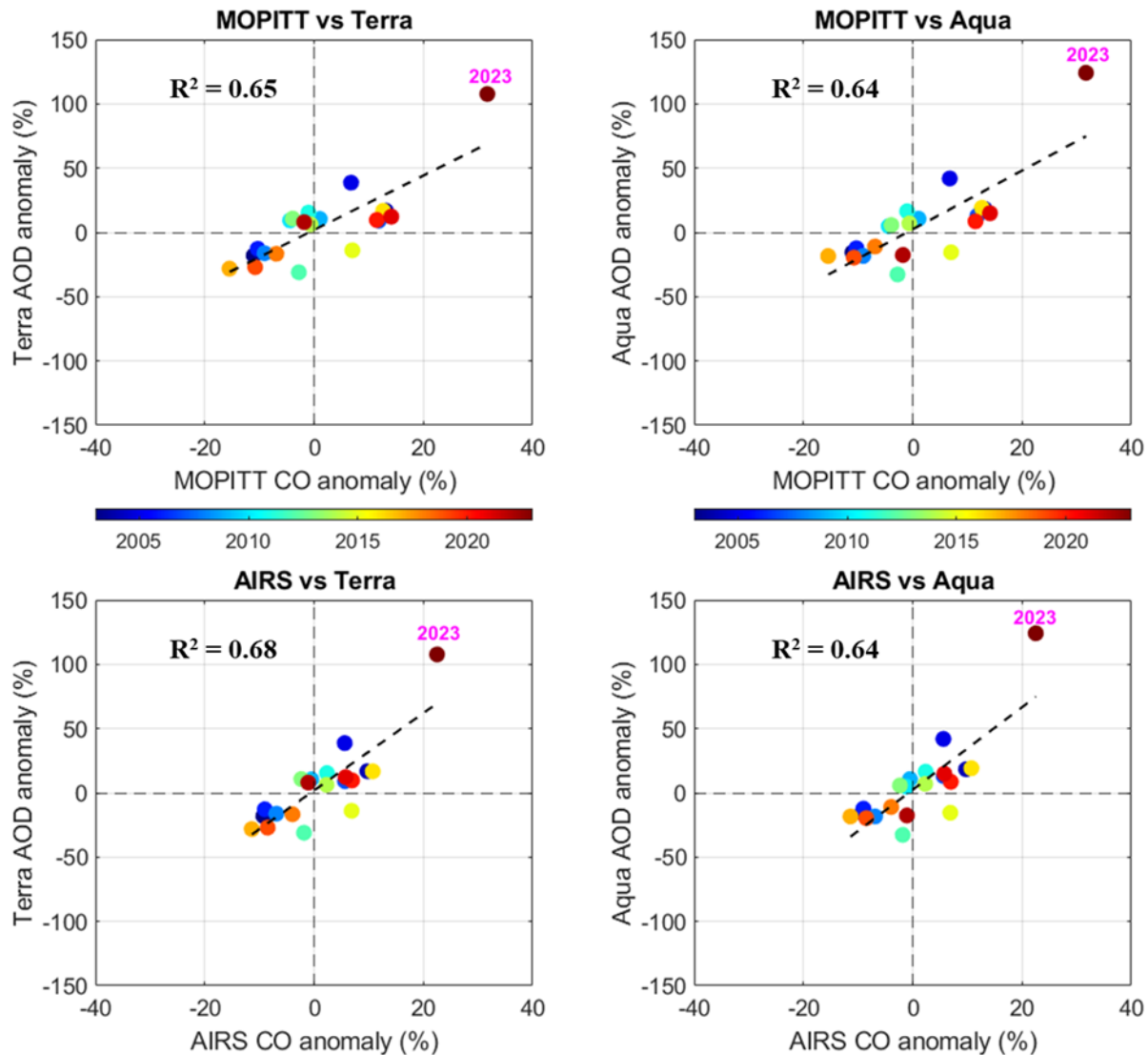
317 The observed CO anomalies from the two satellites are shown in **Fig. 6**, revealing
 318 significantly elevated CO concentrations over the SCS in April 2023, reaching up to 3σ above the
 319 2003–2022 climatology. Although MOPITT displays more spatially concentrated anomalies than
 320 AIRS, both datasets consistently show positive CO anomalies at both pressure levels, indicating a
 321 substantial increase in mid-tropospheric CO during this period. For MOPITT CO retrievals,
 322 primary sources of uncertainty include limitations in vertical sensitivity and potential retrieval
 323 biases (Sayer et al., 2014; Wei et al., 2019). However, the observed enhancements ($>3\sigma$) are
 324 supported by independent AIRS CO measurements, reinforcing the robustness of the detected
 325 anomalies. The comparison between MOPITT and AIRS CO at 500 hPa over the SCS further
 326 shows a strong positive correlation ($R \approx 0.89$; **Fig. S1b** in the Supplement). Furthermore, the

327 spatial distribution of CO anomalies closely resembles that of AOD anomalies (**Fig. 4**). Further,
328 the area-averaged anomalies of AOD and 500 hPa CO over the SCS in April during 2003-2023
329 exhibit a strong positive correlation ($R = 0.81$; **Fig. 7S5 in the Supplement**), suggesting that long-
330 range transport of pollution plays an important role in modulating aerosol variability in this region.
331 The bubble chart further highlights the exceptional severity of the April 2023 event compared with
332 previous years (**Fig. 7S5 in the Supplement**). Because CO is primarily produced by incomplete
333 combustion, elevated concentrations far from major traffic or industrial sources strongly suggest
334 ~~biomass-burning~~BB and wildfire emissions. The strong similarity between the spatial distributions
335 of CO and AOD anomalies suggests that the increased aerosol loading was driven by BB in April
336 2023. This indicates that smoke was likely transported from surrounding regions toward the SCS
337 and the BoB, which are located near major ~~BB~~biomass-burning hotspots, including the MC and
338 PSEA. The MC fire season typically occurs from August to October, whereas PSEA experiences
339 a ~~biomass-burning~~BB season from January to April, peaking in March (**Fig. 2**). These seasonal
340 characteristics strongly suggest that the elevated AOD levels observed over the SCS in April 2023
341 were likely linked to ~~biomass-burning~~BB activity in PSEA. Overall, the April 2023 event is
342 notable for its exceptional intensity and extensive spatial coverage. The MODIS AOD anomalies
343 were approximately four times higher than the long-term mean across much of the SCS and the
344 southern BoB during April 2023. ~~We suggest that this episode represents a rare, previously~~
345 ~~unreported extreme aerosol loading event, distinct from the springtime biomass-burning transport~~
346 ~~events over the PSEA region documented in earlier studies~~. Such anomalously high aerosol
347 loading over the SCS may have important implications for regional climate and hydrological cycle,
348 highlighting the need for further investigation into the underlying drivers and physical mechanisms
349 responsible for this event.



350

351 **Figure 6.** Spatial distribution of carbon monoxide (CO) anomalies in April 2023 at (a) 500 hPa
 352 and (b) 700 hPa from MOPITT satellite measurements. Panels (c) and (d) show the corresponding
 353 CO anomalies at 500 hPa and 700 hPa derived from AIRS satellite observations. Anomalies are
 354 calculated relative to the long-term April mean for 2003–2022. Black dots indicate regions where
 355 anomalies exceed the 3σ significance threshold.



356

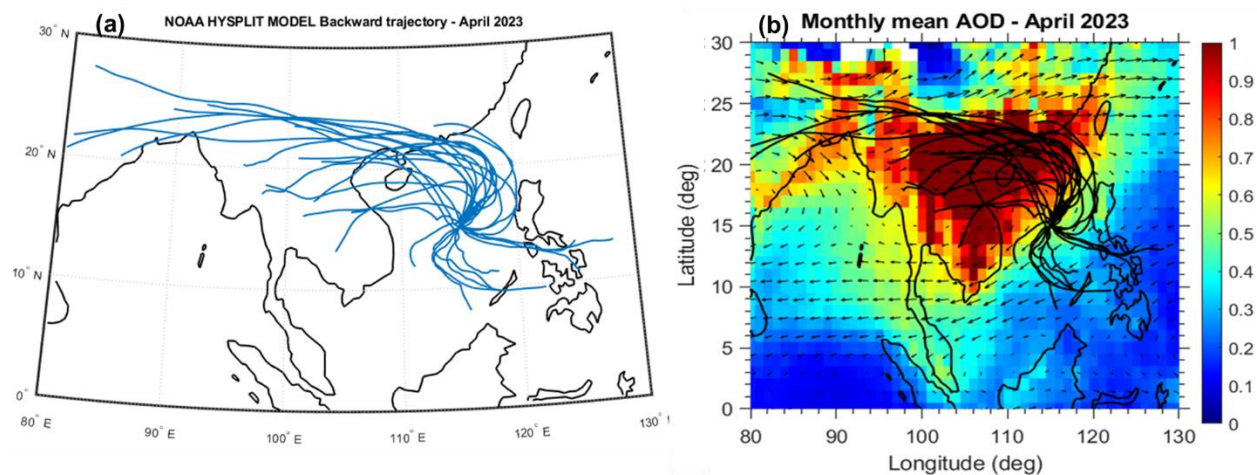
357 Figure 7. Bubble plot of the AOD and CO anomalies (April) over the South China Sea (SCS)
 358 during 2003–2023. Top panels for MOPITT and MODIS (Terra and Aqua), whereas the bottom
 359 panels are for AIRS and MODIS observations. The average coefficient of determination (R^2) is
 360 ~ 0.65 , corresponding to a correlation coefficient (R) of 0.81, indicating a statistically robust
 361 association between CO and AOD over the SCS.

362

363 3.2 Transport and Source Attribution of the April 2023 Aerosol Event

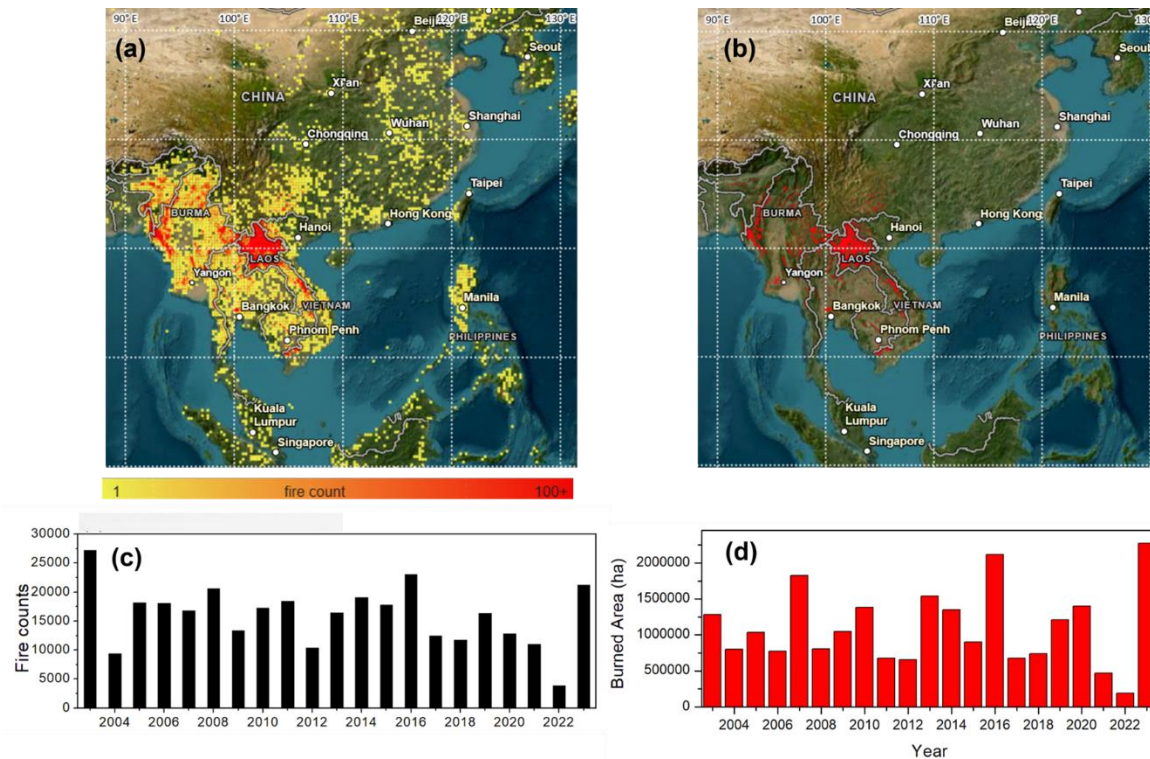
364 From the previous section, it is clear that most aerosols are free-troposphere-dominated
 365 and located primarily in the $\sim 2\text{-}5\text{km}$ region over the SCS. To determine the source regions
 366 responsible for elevated aerosol concentrations over the SCS in April 2023, backward air-mass
 367 trajectories were computed using the NOAA HYSPLIT model. Trajectories were initialized at

368 15°N, 115°E, at 3 km above sea level, corresponding to the altitude range (2--5 km) of the elevated
 369 aerosol layer observed in CALIPSO and MERRA-2 profiles. Daily 72-hour trajectories (Fig. 7a8a)
 370 indicate that air masses arriving over the SCS predominantly originated from northern PSEA.
 371 When overlaid on the monthly mean MODIS AOD (Fig. 7b8b), these trajectories reveal transport
 372 pathways that coincide with regions of high aerosol loading, ~~confirming strongly suggesting~~ that
 373 long-range transport ~~of PSEA BB smoke from northern PSEA likely transported to the SCS. was~~
 374 ~~the primary mechanism delivering BB emissions to the SCS.~~ To examine the BB activity during
 375 April 2023, MODIS fire counts and burned area (BA) data were used. The spatial distributions of
 376 MODIS fire counts and ~~burned area (BA)~~ for April 2023 (Figs. 8a9a–b) show that BB activity
 377 was overwhelmingly concentrated in northern PSEA, particularly in northern Laos and adjacent
 378 regions of Myanmar and Thailand. Minimal fire activity and BA were observed over the MC and
 379 southern China; ~~therefore,~~ these regions were ~~therefore~~ excluded from source-region calculations.
 380 Analysis of inter-annual variability in April BB activity over PSEA from 2003 to 2023 (Figs.
 381 8e9c–d), considering only fire detections above the 80% confidence level, indicates substantial
 382 year-to-year fluctuations. Notably, April 2023 recorded the highest burned area (~2.27 Mha) over
 383 the 21-year period, highlighting the exceptional intensity of BB activity that month.



384
 385 **Figure 78.** (a) Daily 72-h NOAA HYSPLIT backward trajectories ending at 12:00 UTC at a
 386 representative location (15°N, 115°E) over the South China Sea (SCS) at 3 km altitude for April
 387 2023. (b) Same as (a), but overlaid on the monthly mean MODIS aerosol optical depth (AOD) for
 388 April 2023.

389



390

391 **Figure 89.** Spatial distribution of the (a) MODIS fire counts, (b) MODIS Global Burned Area
 392 Product in April 2023. Inter-annual variability in (c) Fire counts, and (d) Burned Area over
 393 Peninsula Southeast Asia in April from 2003 to 2023. (Source:
 394 <https://firms.modaps.eosdis.nasa.gov/>). For inter-annual variability in fire counts, we considered
 395 those above the 80% confidence level.

396 Country-level statistics (**Table 2**) further highlight the dominant contribution from Laos,
 397 which accounted for 11,877 fires (56.0%), 1.53×10^6 MW of fire radiative power (FRP; 63.5%),
 398 and 1.08×10^6 ha of burned area (47.7%). Notably, the BA observed in April 2023 represents the
 399 highest monthly value in the available dataset (2002–2023; **Fig. S6–S5** in the Supplement).
 400 Approximately 60% of Laos is forested (**Fig. S7–S6** in the Supplement), with much of this forest
 401 located in northern Laos where the majority of fires occurred during April 2023 (**Fig. 8a9a**).
 402 Myanmar contributed the second-largest share, with 7,054 fires (33.3%), 7.78×10^5 MW of FRP
 403 (32.3%), and 9.15×10^5 ha of burned area (40.3%). Thailand, Vietnam, and Cambodia contributed
 404 comparatively smaller burned areas of 1.21×10^5 ha, 1.30×10^5 ha, and 2.20×10^4 ha, respectively.
 405 In total, 21,198 fires across PSEA produced approximately 2.41×10^6 MW of FRP in April 2023.
 406 These results strongly suggest that intense BB activity over northern PSEA, likely contributed
 407 substantially to the exceptional aerosol loading observed over the SCS in April 2023. These results
 408 indicate that intense BB activity over northern PSEA, particularly northern Laos, was the primary

409 ~~source of the exceptional aerosol loading observed over the SCS in April 2023.~~ However, two key
 410 questions remain: (i) what factors triggered the anomalously strong fire activity in Laos during
 411 April 2023, and (ii) why were BB aerosols transported unusually far southward across the SCS
 412 and into the southern BoB, rather than following the more typical transport pathways toward
 413 Taiwan and the north western Pacific? To address these questions, we next examine the large-scale
 414 meteorological and dynamical circulation conditions prevailing during April 2023.

415 **Table 2.** MODIS total fire counts, the corresponding total accumulated fire radiative power (FRP),
 416 and the burned area (BA) observed over peninsular Southeast Asia (PSEA) and each country
 417 within PSEA in April 2023. The percentage contribution of each country to the total number of
 418 fires, the total FRP, and the BA of PSEA is shown in brackets.

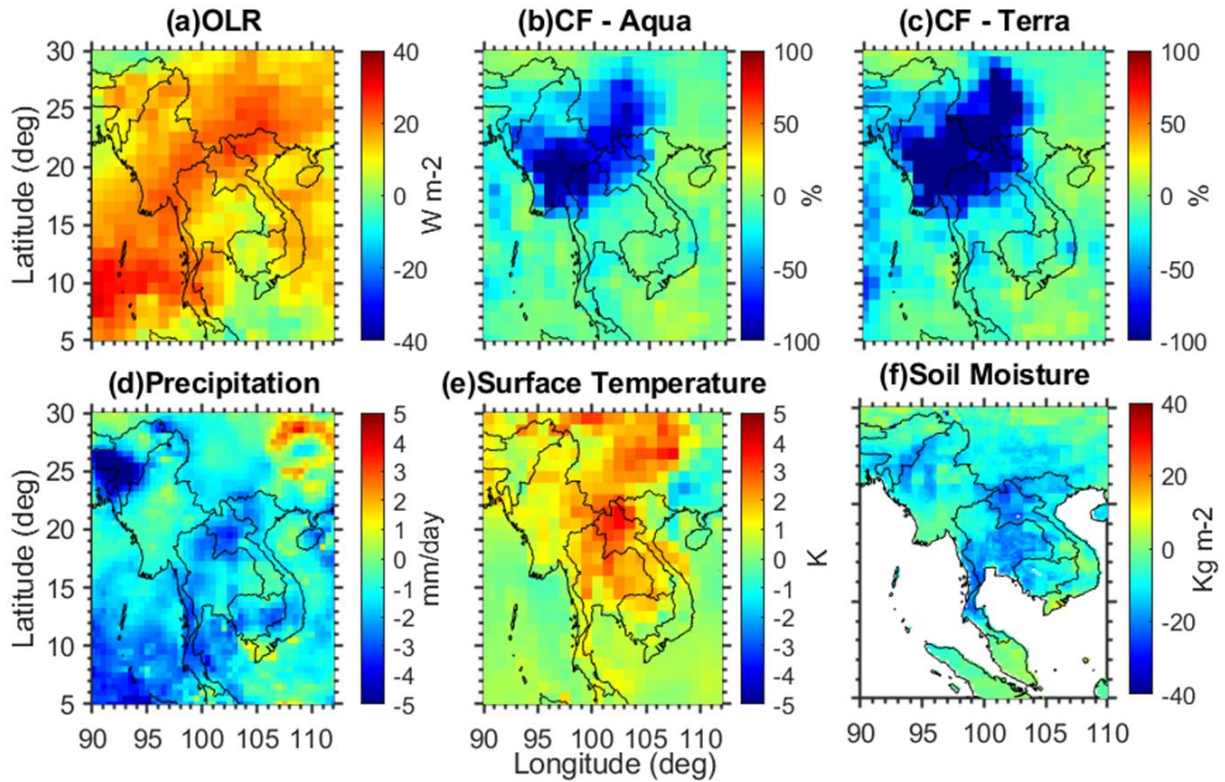
Country	Total Fires	Fire Radiative Power (MW)	Burned Area (ha)
PSEA	21198	2407283	2272099.89
Country	Total Fires	FRP	BA
Cambodia	242 (1.14%)	13402 (0.5%)	21959.5 (0.97%)
Laos	11877 (56.02%)	1530000 (63.5%)	1084050 (47.71%)
Myanmar	7054 (33.27%)	777970 (32.32%)	915175.7 (40.27%)
Thailand	1322 (6.24%)	50276 (2.1%)	120573.7 (5.31%)
Vietnam	703 (3.32%)	35634 (1.5%)	130340.7 (5.74%)

419

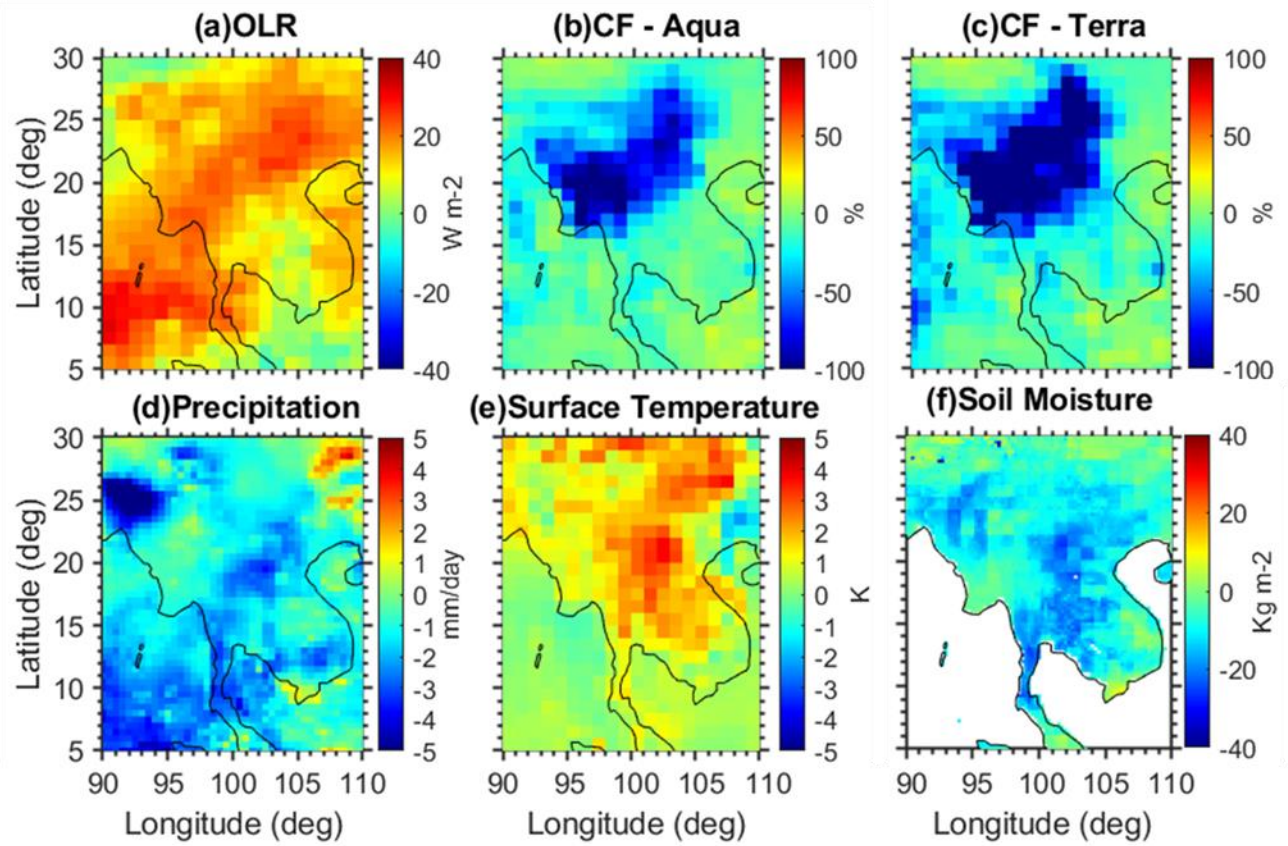
420 3.3 Large-scale meteorological and dynamical circulation anomalies in April 2023

421 In this section, we examine the meteorological and large-scale dynamical circulation
 422 anomalies associated with the April 2023 event. **Figure 9-10** presents the spatial distribution of
 423 anomalies in key meteorological parameters during April 2023 relative to the 2003–2022
 424 climatological mean. As shown in **Figure 9-10**, ~~anomalies in~~ Outgoing Longwave Radiation (OLR)
 425 ~~anomalies~~ indicate suppressed convective activity over PSEA during April 2023. Reduced
 426 convection was accompanied by negative precipitation anomalies, elevated surface temperatures,
 427 and pronounced soil moisture (SM) deficits. These conditions are spatially consistent with the

428 regions of enhanced fire counts and ~~burned-area~~BA observed by MODIS over northern Laos (**Fig.**
429 **89**). Long-term SM anomalies over northern Laos reached exceptionally low values in April 2023,
430 representing the lowest levels in the past two decades (**Figs. S8a**S7a–b in the Supplement). To
431 further examine the persistence of these conditions, we analyzed the temporal evolution of SM
432 anomalies during 2021–2023. The results show maximum positive anomalies in March 2022 and
433 a transition to strong negative anomalies by April 2023, indicating a prolonged drought from
434 winter 2022 to April 2023 (**Fig. S8c**S7c in the Supplement). We further assessed the relationship
435 between SM anomalies and fire activity over Laos. Standardized fire anomalies and SM anomalies
436 (**Fig. S9**S8 in the Supplement) reveal a significant inverse relationship: reduced SM is associated
437 with enhanced fire activity. In April 2023, extreme negative SM anomalies coincided with strong
438 positive fire anomalies, highlighting the role of severe surface drying in promoting intense
439 ~~biomass-burning~~BB activity. A similar co-occurrence of anomalously low SM and elevated fire
440 activity is also evident in 2016, a year previously identified as having intensified regional burning.
441 These findings provide additional observational evidence that ~~soil-moisture~~SM deficits are linked
442 to enhanced fire activity over PSEA. Previous studies have shown that negative SM anomalies can
443 promote positive geopotential height anomalies in the upper troposphere, which tend to reinforce
444 local high-pressure conditions and enhance surface warming (e.g., Fischer et al., 2007; Dong et
445 al., 2023). Motivated by this mechanism, we next examine the large-scale dynamical circulation
446 patterns during April 2023 to understand how atmospheric dynamics may have contributed to the
447 observed meteorological anomalies and the anomalous transport of ~~biomass-burning~~BB aerosols.

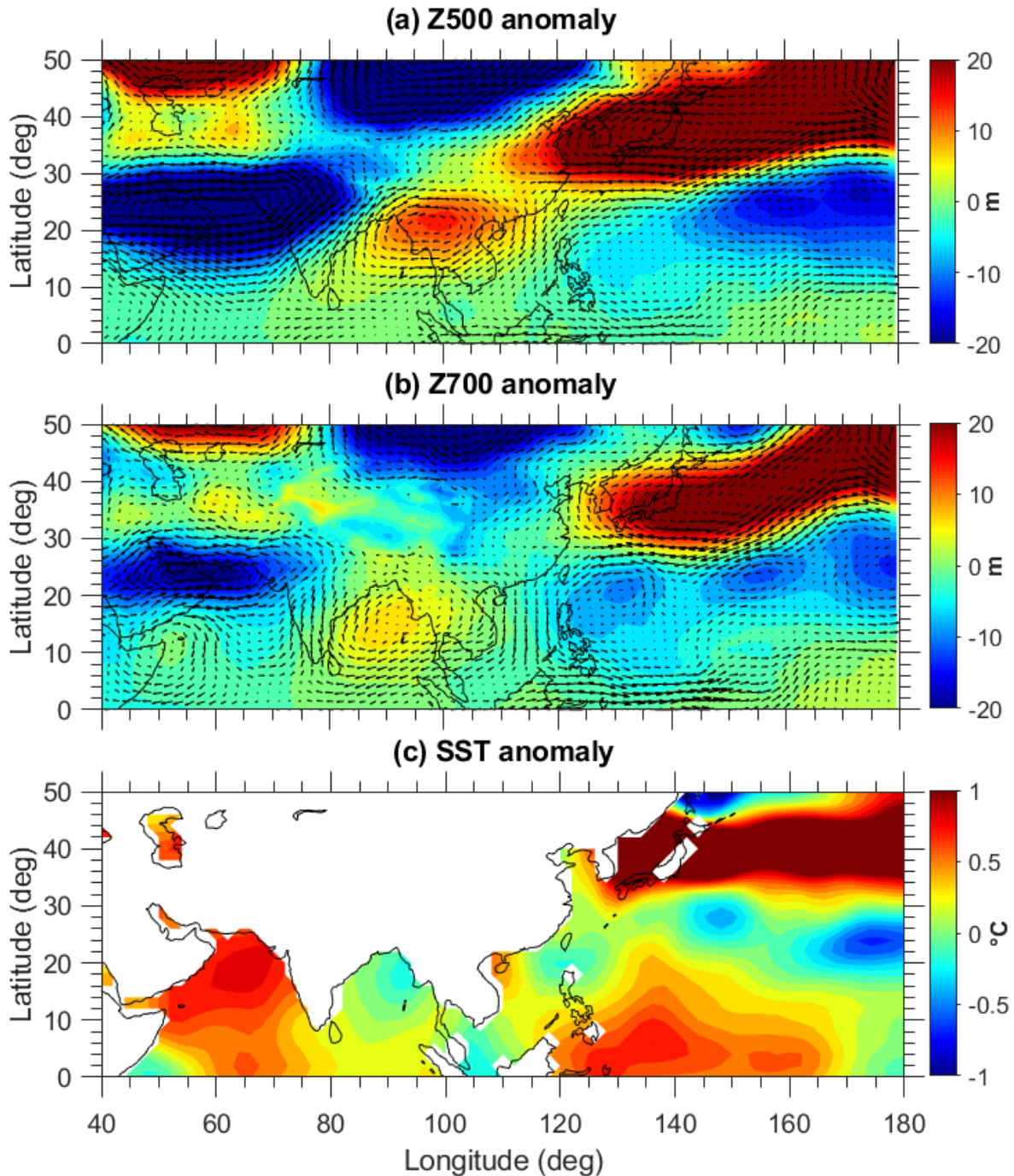


448



449

450 **Figure 910.** Surface and atmosphere conditions in April 2023. April anomalies in 2023 compared
451 to the 2003-2022 climatological period for (a) Outgoing Longwave radiation (OLR), (b) cloud
452 fraction (CF) from Aqua, (c) cloud fraction from Terra, (d) precipitation, (e) Surface Temperature,
453 (f) soil moisture (10 - 40 cm underground). OLR and surface temperatures are obtained from AIRS
454 satellite measurements. CF data from MODIS Aqua and Terra. Soil moisture is obtained from the
455 GLDAS Noah Land Surface Model L4 monthly 0.25 x 0.25 degree V2.1. Precipitation data is
456 obtained from the Global Precipitation Climatology Project (GPCP) Version 3.2.



457

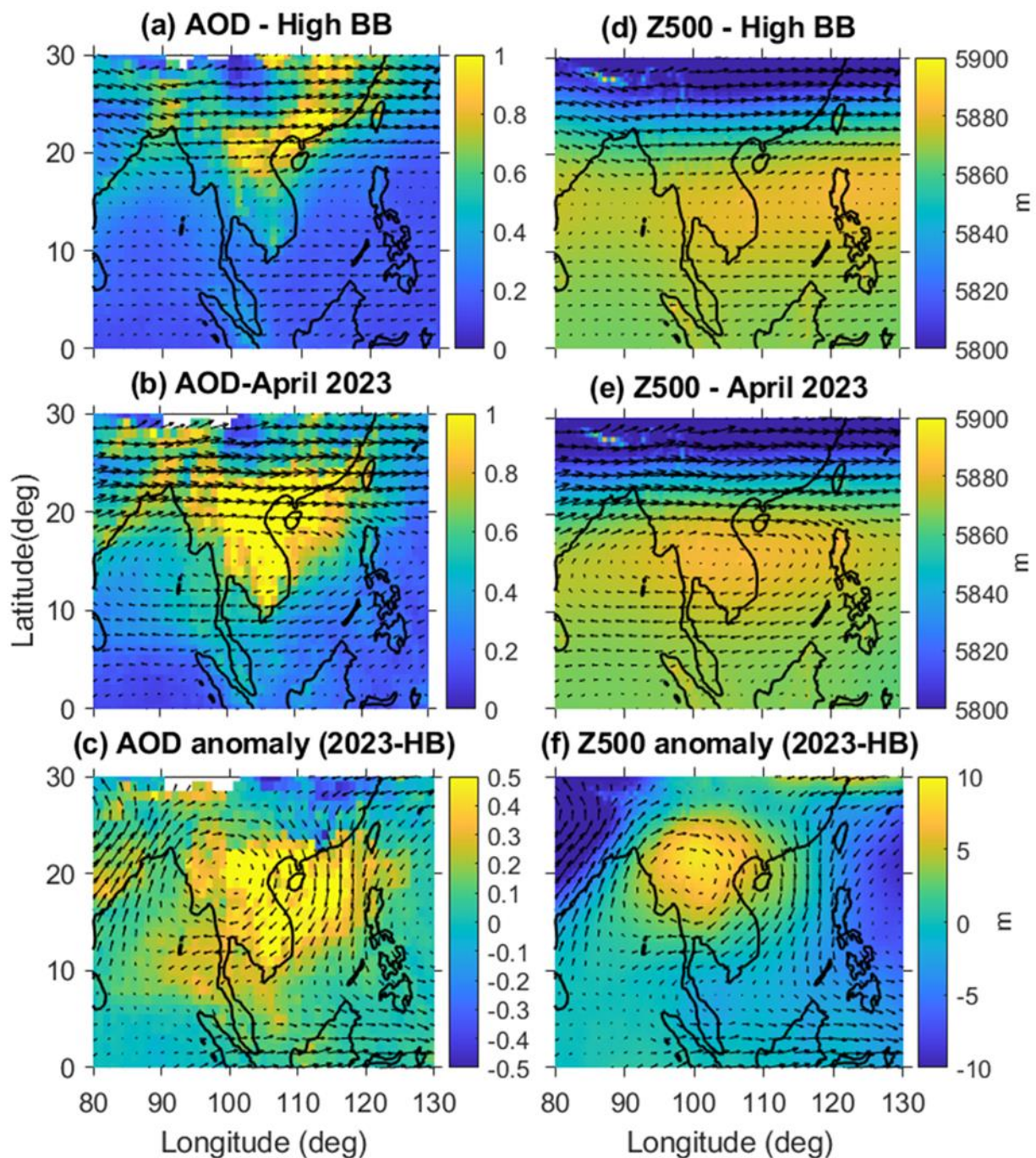
458 **Figure 1011.** Spatial distribution of (a) 500 hPa geopotential height (Z500), (b) 700 hPa
459 geopotential height (Z700), and (c) Sea Surface Temperature (SST) anomalies in April 2023. The
460 anomalies are calculated by subtracting the April 2023 monthly mean from the April climatology
461 for the period 1991 to 2020. The wind anomalies for the respective pressure levels are overlaid in
462 Z500 and Z700 anomalies. The geopotential height and wind data are from the MERRA-2
463 reanalysis, while SST data are from the NOAA Extended Reconstructed SST V5.

464
465 Our analysis focuses on geopotential height and horizontal wind fields at the 700- and 500-
466 hPa levels. The geopotential height fields (Z700 and Z500) in April 2023 show clear departures
467 from the April climatology (1991-2020) (**Figs. S10S9–11-10** in the Supplement). At 700 hPa, the
468 climatological high-pressure system over the Indian region extended eastward toward PSEA, while
469 at 500 hPa, the western Pacific subtropical anticyclone shifted westward to lie directly over PSEA.
470 Geopotential height anomalies relative to the 1991–2020 mean (**Fig. 10a11a-b-b**) reveal a
471 pronounced anti-cyclonic circulation (positive anomalies) centered over northern PSEA (~20°N,
472 100°E) at 500 hPa. Similar anti-cyclonic anomalies are also evident in the Z700 field over the
473 BoB. At the same time, significant cyclonic anomalies (negative geopotential height anomalies)
474 are observed over the Arabian Sea and the WNP at both levels. These geopotential height anomaly
475 patterns are broadly consistent with the observed sea surface temperature (SST) anomaly
476 distribution. Positive SST anomalies are evident over the Arabian Sea, whereas negative SST
477 anomalies occur over the BoB (Fig. 11). Positive SST anomalies are also observed over the WNP
478 warm pool region, where negative geopotential height anomalies are present. Collectively, these
479 patterns suggest a low–high–low (L–H–L)-like wave train extending from the Arabian Sea to the
480 WNP warm pool region. These findings are consistent with those of Liu et al. (2026), who
481 proposed that enhanced convection over the Horn of Africa and Arabian Peninsula (HAAP)
482 generated downstream Rossby wave propagation across South Asia and mainland Southeast Asia,
483 contributing to anomalous upper-level cyclonic circulation over South Asia and anti-cyclonic
484 circulation over the Indochina Peninsula (ICP) and southern China. However, their analysis was
485 primarily based on upper-tropospheric (~300 hPa) circulation fields. Although our analysis focuses
486 on mid-tropospheric circulation anomalies at 700 and 500 hPa, the observed patterns are broadly
487 consistent with a vertically coherent large-scale circulation response during spring 2023. These
488 circulation anomalies, particularly mid-tropospheric anti-cyclone that suppressed convection over
489 PSEA, are consistent with positive OLR anomalies and reduced precipitation (Fig. 910).

490 Subsidence associated with the anti-cyclonic circulation promoted clear-sky conditions (**Fig. 910**)
491 and surface warming, which, together with severe soil moisture deficits, created favorable
492 conditions for intense ~~biomass burning~~BB across northern Laos. Liu et al. (2026) further showed
493 that upper-tropospheric convergence and dynamical subsidence associated with this wave pattern
494 contributed to persistent heat and drying over the ICP during spring 2023, potentially supporting
495 the lower- and mid-tropospheric anti-cyclonic anomalies identified here. The circulation pattern
496 also altered regional transport pathways. The combined influence of the WNP cyclone, the BoB
497 anticyclone at 700 hPa, and the PSEA anticyclone at 500 hPa modified the background flow over
498 Southeast Asia. Meridional wind anomalies (**Figs. S12bS11b–c** in the Supplement) show
499 persistent northerly flow over the SCS, enabling southward transport of smoke from northern
500 PSEA toward the SCS and into the southern BoB. ~~This pathway contrasts with the climatological~~
501 ~~transport route that typically advects smoke toward Taiwan and the northwestern Pacific.~~ Zonal
502 wind anomalies further indicate weakened mid-latitude westerlies and locally reversed easterlies
503 near Japan and Taiwan associated with a strong anti-cyclonic anomaly (**Figs. S12aS11a–b** in the
504 Supplement), suppressing the typical eastward transport of smoke. Consistent with this, AOD
505 observations from the high-altitude mountain background station, namely Lulin Atmospheric
506 Background Station (LABS) obtained through AERONET show no notable enhancement in April
507 2023 (**Fig. S13a–S12** in the Supplement), indicating reduced smoke transport toward the
508 northwestern Pacific. AERONET comparisons show strong correlations with MODIS AOD: 0.83
509 for Aqua and 0.84 for Terra (**Fig. S14S13** in the Supplement), further supporting the reliability of
510 the satellite observations as shown in the Dongsha data. Overall, the anomalous circulation pattern,
511 characterized by a BoB anticyclone and a WNP cyclone, redirected BB plumes from northern
512 PSEA toward the SCS and southern BoB, producing the exceptional aerosol loading observed in
513 April 2023.

514 A key question is whether April 2023 represents was an exceptional ~~biomass burning~~(BB)
515 year relative to PSEA, or if-whether similar conditions have occurred in other high-BB years.
516 High-BB years were identified using standardized fire anomalies derived from April MODIS fire
517 counts following the method of Vadrevu et al. (2019). For this analysis, April fire counts from
518 2003–2023 were standardized relative to the 2003–2022 climatology over northern PSEA (17–
519 23°N). Years with anomaly values exceeding 0.5 were classified as high-BB years (Fig. S14),
520 including 2003, 2006, 2008, 2010, 2014, 2015, 2016, and 2023. Composite analyses of MODIS

521 AOD, 500 hPa geopotential height (Z500), and wind vectors were conducted to characterize
522 typical aerosol and circulation patterns during high-BB conditions. **Figure 12a–c** presents the
523 spatial distributions of composite AOD for high-BB years, AOD during April 2023, and their
524 anomalies, respectively, while **Fig. 12d–f** shows the corresponding Z500 and wind vector fields.
525 Relative to the high-BB composite, April 2023 exhibited substantially higher AOD across PSEA,
526 the SCS, and the southern BoB, indicating enhanced regional aerosol loading. The Z500 field
527 further showed pronounced positive anomalies over northern PSEA, reflecting a stronger, more
528 spatially coherent anti-cyclonic circulation than under typical high-BB conditions.
529 Correspondingly, wind anomalies revealed enhanced northerly flow over the SCS during 2023,
530 suggesting strengthened meridional aerosol transport. An additional comparison between April
531 2016 and April 2023 (**Fig. S15** in the supplement) showed similar spatial patterns, including
532 enhanced AOD over southern PSEA. However, the magnitude and spatial extent of the AOD
533 enhancement were greater in 2023. The AOD anomaly between 2023 and 2016 further revealed
534 pronounced increases over the SCS and southern BoB, coinciding with enhanced northerly
535 anomalies. Overall, these results suggest that anomalous circulation conditions in 2023 likely
536 amplified aerosol transport and accumulation beyond those typically associated with high-BB
537 years.



538

539 ~~High BB years were identified using standardized fire anomalies from MODIS fire counts, with~~
 540 ~~years exceeding 0.5 classified as high BB (Fig. S9 in the Supplement). Composites of MODIS~~
 541 ~~AOD, 500-hPa geopotential height, and wind vectors were constructed to represent typical~~
 542 ~~circulation and aerosol patterns during high-BB periods. Comparison with April 2023 shows~~
 543 ~~notable differences: 2023 featured a stronger, more spatially coherent anti-cyclonic high over~~
 544 ~~PSEA and substantially higher AOD, indicating unusually intense aerosol loading. This suggests~~
 545 ~~that circulation anomalies in 2023 amplified aerosol accumulation and transport beyond typical~~
 546 ~~high-BB conditions (Fig. S15 in the Supplement).~~ **Figure 12. Spatial distribution of MODIS**

547 aerosol optical depth (AOD), MERRA-2 500-hPa geopotential height (Z500), and wind vectors
548 during April. (a) Composite AOD for high biomass-burning (BB) years, (b) AOD in 2023, and (c)
549 AOD anomalies between 2023 and the composite high-BB years. Panels (d–f) show the
550 corresponding composites for Z500 and associated wind vectors for (d) high-BB years, (e) 2023,
551 and (f) anomalies between 2023 and the high-BB composite, respectively.

552
553 Another question is whether inter-annual variability associated with climate oscillations,
554 such as the El Niño–Southern Oscillation (ENSO), influenced BB activity and circulation in 2023.
555 SST anomalies ~~linked to~~associated with ENSO strongly modulate Indo-Pacific circulation and
556 hydro–climate, with El Niño events typically enhancing springtime fires ~~via~~through drought,
557 reduced precipitation, and suppressed moisture transport (Yin, 2020; Zhu et al., 2021; Zheng et
558 al., 2023). We constructed composites of MODIS AOD and 500-hPa wind vectors for El Niño–
559 ensuing and La Niña–ensuing Aprils during 2003–2022 (**Fig. S16** in the Supplement). The results
560 reveal higher AOD over northern PSEA and coastal South China during El Niño-ensuing Aprils,
561 accompanied by a stronger anti-cyclonic system over PSEA extending from the BoB, consistent
562 with enhanced aerosol accumulation. In contrast, Aprils following La Niña show weaker
563 circulation and lower AOD. April 2023 occurred during the transition from a triple-dip La Niña to
564 a developing El Niño, deviating from typical ENSO-fire patterns. This unusually large-scale
565 background is consistent with Liu et al. (2026), who noted that the extreme spring 2023 heat event
566 over the ICP differed fundamentally from canonical ENSO-linked events, as severe regional
567 warming and subsidence developed despite antecedent La Niña conditions.

568 Overall, systematic analysis of MODIS fire counts, burned area (BA), HYSPLIT back
569 trajectories, and MERRA-2 large-scale circulation fields, we conclude that the extreme aerosol
570 event in April 2023 was shaped not only by BB activity but also by anomalous large-scale
571 circulation patterns. These findings highlight the combined influence of BB emissions and
572 background meteorological conditions in producing the exceptional smoke event.

573 ~~The anomalous anti-cyclonic and cyclonic circulations over the BoB and western North Pacific in~~
574 ~~April 2023 are notable (Fig. 10), though their detailed dynamics are beyond the scope of this study.~~
575 ~~Preliminary analysis revealed that SST warming over the western Pacific warm pool and mid-~~
576 ~~latitude North Pacific, together with cooling over the central-eastern equatorial Pacific, likely~~
577 ~~induced a Matsuno–Gill type response, while warming in the Arabian Sea and cooling in the BoB~~
578 ~~aligned with geopotential height anomalies, promoting drought, intensified BB, and southward~~

579 ~~smoke transport toward the SCS and southern BoB (Fig. 10c; Gill, 1980; Zeng and Sun, 2022).~~
580 ~~Overall, the extreme aerosol event in April 2023 was shaped not only by intense biomass burning~~
581 ~~but also by anomalous large-scale circulation linked to ocean-atmosphere variability, highlighting~~
582 ~~the combined role of local and climate-scale drivers in exceptional smoke events.~~

583 **4. Summary and Conclusions**

584 In April 2023, record-breaking aerosol loading was observed over the South China Sea
585 (SCS). By integrating multiple satellite measurements (MODIS, MOPITT, AIRS, and CALIPSO),
586 the MERRA-2 reanalysis, and NOAA HYSPLIT back-trajectory analysis, we systematically
587 investigated the sources, transport pathways, and large-scale dynamical conditions associated with
588 this extreme event. MODIS observations indicate an approximately 150% increase in aerosol
589 optical depth (AOD), relative to the long-term mean (2003-2022). This enhancement was
590 accompanied by pronounced increases in carbon monoxide (CO) in the mid- to lower troposphere
591 (700–500 hPa) as observed by MOPITT and AIRS, consistent with long-range transport of
592 combustion-related pollution. The simultaneous increases in AOD and CO over the remote ocean
593 support the influence of transported biomass-burning (BB) emissions from surrounding source
594 regions. Analysis of MODIS fire counts and burned area revealed a significant enhancement in
595 BB activity over northern PSEA and negligible BB activity over South China and the Maritime
596 Continent. Furthermore, NOAA HYSPLIT back trajectories indicate that most air masses over the
597 SCS originate from the northern PSEA. Together, fire counts, BA, and HYSPLIT trajectory
598 analysis suggest that enhanced BB activity over northern PSEA likely contributed to the
599 exceptional aerosol loading over the SCS in April 2023. Meteorological conditions characterized
600 by suppressed convection, reduced precipitation, elevated surface temperatures, and decreased soil
601 moisture likely promoted increased BB activity. These conditions were associated with a
602 pronounced high-pressure (anti-cyclonic) anomaly over PSEA, as indicated by positive
603 geopotential height anomalies at 500 hPa (Figure 11a).

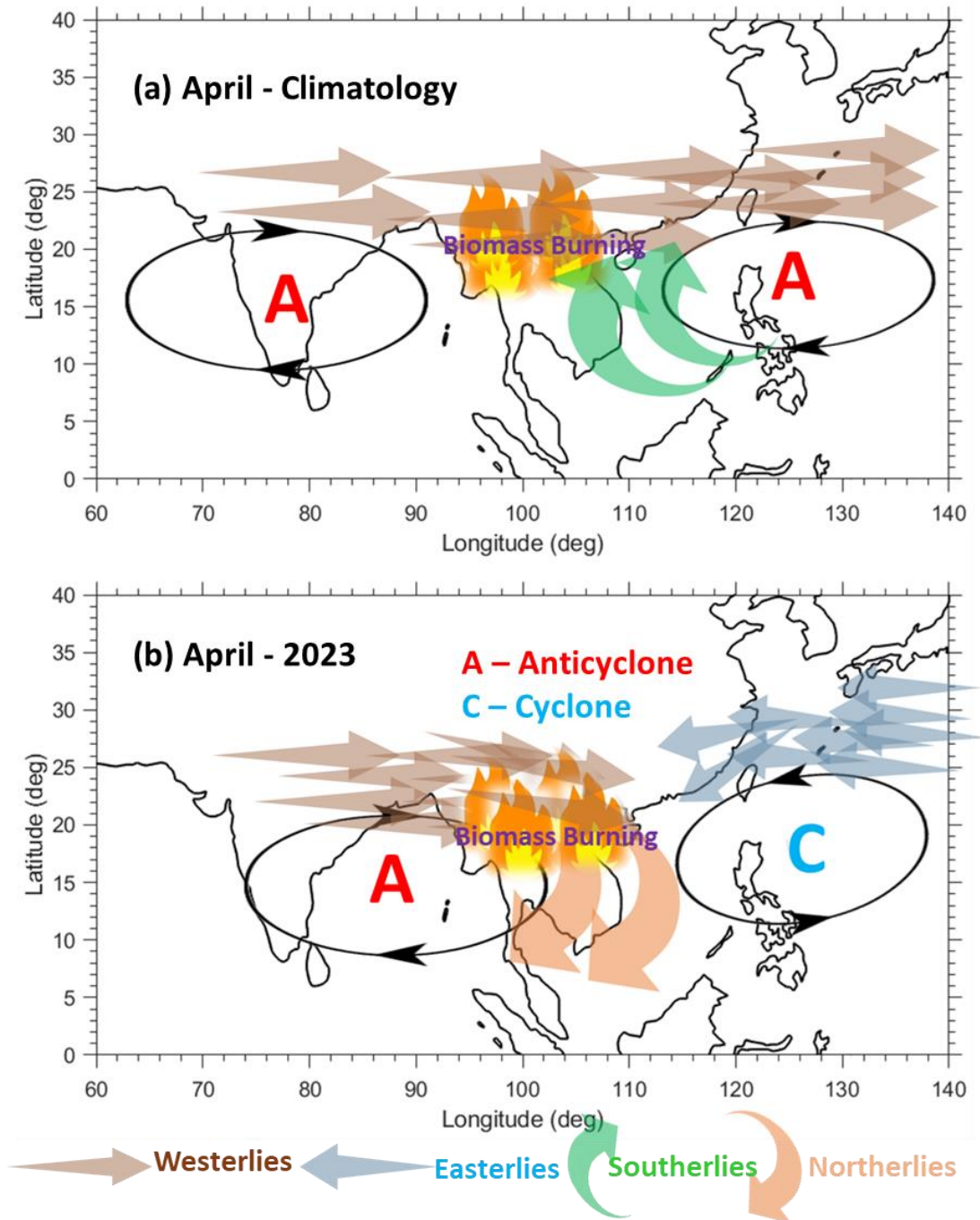
604 Large-scale circulation analyses further reveal a free-tropospheric pattern featuring an
605 eastward-shifted Bay of Bengal (BoB) anticyclone and a western North Pacific (WNP) cyclone
606 (Figure 11b). These circulation features significantly modified regional flow over the SCS by
607 reversing the prevailing meridional winds from southerly to northerly anomalies. In addition, the
608 coexistence of a subtropical anticyclone over the northwestern Pacific and the WNP anomaly

609 generated easterly wind anomalies around Taiwan. Together, these anomalous circulation patterns
610 altered BB smoke transport pathways and facilitated aerosol accumulation over the SCS in April
611 2023. A schematic summary of the physical mechanisms is provided in **Figure 13**.

612 ~~In April 2023, we observed an unprecedented increase in aerosol loading over the South~~
613 ~~China Sea (SCS), which had not been recorded during the two-decade MODIS satellite~~
614 ~~measurements period from 2003 to 2023. Satellite observations revealed ~150% increase in AOD~~
615 ~~(MODIS), approximately four times higher than the long-term mean, alongside significant~~
616 ~~enhancements in CO (MOPITT and AIRS) at the 700 and 500 hPa levels. This study investigates~~
617 ~~the causes, physical mechanisms, and atmospheric dynamics underlying this extraordinary aerosol~~
618 ~~event. Analyses of satellite data (MODIS, MOPITT, AIRS, and CALIPSO), NOAA HYSPLIT~~
619 ~~back-trajectories, and MERRA-2 reanalysis products indicate that intense biomass-burning activity~~
620 ~~over northern Peninsular Southeast Asia was the primary driver of the record-breaking aerosol~~
621 ~~loading over the SCS in April 2023. Our results further reveal that this BB activity was amplified~~
622 ~~by exceptional meteorological conditions associated with unusually large-scale dynamical~~
623 ~~circulation patterns. A dominant anti-cyclonic anomaly over PSEA suppressed convection, leading~~
624 ~~to subsidence, elevated surface temperatures, and drought conditions that fueled fires, particularly~~
625 ~~in Laos and Myanmar, which contributed most to the regional BB emissions. A schematic~~
626 ~~summarizing these drivers and mechanisms is presented in **Figure 11**.~~

627 ~~Climatologically, two anti-cyclones are typically situated over the WNP and the Indian~~
628 ~~Ocean, producing predominantly southwesterly and southerly winds over the SCS. These southerly~~
629 ~~winds generally transport BB smoke from PSEA to downwind regions such as Taiwan and the~~
630 ~~WNP. In April 2023, however, the WNP anticyclone transformed into a cyclone, while the Indian~~
631 ~~Ocean anticyclone shifted eastward over the BoB near PSEA. The resulting northerly flow over~~
632 ~~the SCS, combined with easterly anomalies near Taiwan, blocked transport toward the~~
633 ~~northwestern Pacific and redirected smoke from PSEA to the SCS and BoB. This circulation shift,~~
634 ~~driven by the combined WNP cyclone and BoB anticyclone, highlights the critical role of large-~~
635 ~~scale atmospheric dynamics in determining BB smoke pathways. These findings improve~~
636 ~~understanding of transboundary pollution and can inform regional monitoring efforts over PSEA.~~

637



638

639 **Figure 13.** Schematic diagram illustrating the physical mechanisms responsible for the record-
 640 breaking aerosol loading over the South China Sea (SCS) in April 2023. The diagram summarizes
 641 the anomalous circulation and transport pathways governing biomass-burning (BB) smoke
 642 distribution. Here, ‘A’ denotes an anticyclone anomaly and ‘C’ denotes a cyclone anomaly.
 643 Horizontal arrows represent subtropical free-tropospheric westerlies and easterlies, while green
 644 and brown arrows indicate southerly and northerly winds, respectively. Top panel: The
 645 climatological conditions in April (1991-2020), characterized by the Bay of Bengal (BoB) and

646 western Pacific anticyclones, as well as prevailing southwesterly and southerly winds over the
647 SCS that favor typical smoke transport toward Taiwan and the western North Pacific (WNP).
648 Bottom panel: April 2023 conditions, featuring a WNP cyclone, and an eastward-shifted BoB
649 anticyclone. These anomalies generated persistent northerly winds over the SCS and redirected
650 BB plumes toward the SCS and the southern BoB. Strengthened easterlies around Taiwan further
651 inhibited eastward transport, resulting in exceptional aerosol accumulation over the SCS in April
652 2023.

653 While this study focuses on the sources, transport pathways, and dynamical drivers of the
654 record aerosol event, its broader impacts remain to be quantified. In particular, aerosol–radiation
655 interactions associated with elevated AOD may significantly affect regional radiative forcing,
656 atmospheric heating profiles, and the hydrological cycle. Future work will quantify the radiative
657 impacts of these extreme aerosol concentrations and assess their implications for regional climate.
658 Additionally, elevated BB emissions of CO and other precursors may enhance tropospheric ozone
659 formation, a topic that warrants further investigation. Notably, mainland Southeast Asia
660 experienced an extreme heatwave in April 2023, with record-high temperatures (Zachariah et al.,
661 2024; Lyu et al., 2024). While previous studies attribute this event to anthropogenic climate
662 change, strengthened high-pressure systems, and land–atmosphere coupling, our results suggest
663 that BB aerosols and associated greenhouse gas emissions may also have contributed to the
664 regional heat anomaly. Key outstanding questions include how BB-derived greenhouse gases
665 influence regional radiative trapping and how elevated aerosol concentrations modify surface
666 radiation, cloud processes, and precipitation. Addressing these questions is essential for
667 understanding compound climate extremes in PSEA and surrounding regions. In conclusion, this
668 study highlights the combined role of BB emissions and large-scale dynamical conditions in
669 shaping smoke transport over Southeast Asia, providing deeper insights into the mechanisms
670 governing extreme regional aerosol events.

671
672 ~~While the present study focuses on the record breaking aerosol loading, its sources, transport~~
673 ~~pathways, and dynamical drivers, the broader impacts of this extreme event remain largely~~
674 ~~unexplored. In particular, aerosol–radiation interactions associated with such unusually high AOD~~
675 ~~could substantially affect regional energy balance, atmospheric heating profiles, and the~~
676 ~~hydrological cycle over adjacent regions. Future research will aim to quantify the radiative forcing~~
677 ~~of these extreme aerosol concentrations and assess their broader atmospheric impacts.~~
678 ~~Additionally, the exceptional increase in CO and other BB emissions may have strong implications~~
679 ~~for tropospheric ozone formation, which will also be investigated. Interestingly, PSEA~~
680 ~~experienced an extreme heatwave in April 2023, with record-high temperatures (Zachariah et al.,~~

2024; Lyu et al., 2024). Previous studies have attributed this heatwave to climate change (Zachariah et al., 2024), as well as strengthened high pressure systems, moisture deficits, and strong land-atmosphere coupling (Lyu et al., 2024). Our results suggest a plausible contribution from biomass burning aerosols and associated greenhouse gases to this heatwave. Key questions for future investigation include: How do greenhouse gases released by record-breaking BB activity influence regional heat trapping? What is the impact of elevated aerosol concentrations on surface radiation, cloud formation, and precipitation patterns? Addressing these questions will be critical to understanding the exceptional conditions in PSEA and surrounding regions, including the combined effects of BB aerosols and greenhouse gas emissions on regional climate extremes.

Code and data availability

This study exclusively utilized publicly available datasets, and no new observational data were generated. All data required to evaluate the conclusions of this study are included in the paper and/or the Supplementary Information. Most figures presented in this study were generated using MATLAB R2020a. All datasets used in the study are freely available for download from their respective websites. **Data availability**

MODIS data available from <https://modis.gsfc.nasa.gov/data/dataproduct/mod08.php>. The AIRS and MOPITT CO data can be downloaded from https://disc.gsfc.nasa.gov/datasets/AIRS3STM_7.0 (AIRS project, 2019) and https://asdc.larc.nasa.gov/project/MOPITT/MOP02J_8 (NASA, 2023a). MERRA-2 data are available online through the NASA Goddard Earth Sciences Data Information Services Center (GES DISC; <https://disc.gsfc.nasa.gov>; NASA, 2023b). The MODIS fire and burned area products can be downloaded from https://firms.modaps.eosdis.nasa.gov/active_fire/ (NASA, 2023c). Daily CALIPSO vertical distribution images of various aerosol types were obtained from <https://www-calipso.larc.nasa.gov/products>. The NOAA HYSPLIT back trajectories are retrieved from <https://www.ready.noaa.gov/HYSPLIT.php>.

Author Contributions

Saginela Ravindra BabuSRB: Conceptualization, Data curation, Formal analysis, Investigation, Software, Validation, Visualization, Writing – original draft preparation, Writing – review and

712 editing; ~~N-HLNeng-Huei—Lin~~: Conceptualization, Investigation, Funding Acquisition,
713 Supervision, Resources, Writing – review and editing.

714 **Competing interests**

715 The authors declare no competing interests.

716 **Acknowledgements**

717 We acknowledge the National Science and Technology Council of Taiwan for supporting the
718 research under grant 114-2111-M-008-030. The authors thank NASA and NOAA for providing
719 MOPITT, MODIS, CALIPSO and AIRS satellite data. We thank NASA's Global Monitoring and
720 Assimilation Office (GMAO) for providing the Modern-Era Retrospective analysis for Research
721 and Applications, Version 2 (MERRA-2) data.

722

723

724

725

726 **References**

727 Anderson, T. L., Charlson, R. J., Schwartz, S. E., Knutti, R., Boucher, O., Rodhe, H., and
728 Heintzenberg, J.: Climate forcing by aerosol– a hazy picture, *Science*, 300, 1103–1104,
729 <https://doi.org/10.1126/science.1084777>, 2003.

730 AIRS Project. Aqua/AIRS L3 Monthly Standard Physical Retrieval (AIRS-only) 1 degree x 1
731 degree V7.0 [Data set]. NASA Goddard Earth Sciences Data and Information Services Center.
732 <https://doi.org/10.5067/UBENJB9D3T2H>, 2020.

733 Buchholz, R. R., Worden, H. M., Park, M., Francis, G., Deeter, M. N., Edwards, D. P., Emmons,
734 L. K., Gaubert, B., Gille, J., Martinez-Alonso, S., Tang, W., Kumar, R., Drummond, J. R.,
735 Clerbaux, C., George, M., Coheur, P.-F., Hurtmans, D., Bowman, K. W., Luo, M., Payne, V. H.,
736 Worden, J. R., Chin, M., Levy, R. C., Warner, J., Wei, Z., and Kulawik, S. S.: Air pollution trends
737 measured from Terra: CO and AOD over industrial, fire-prone, and background regions, *Remote*
738 *Sens. Environ.*, 256, 112275, <https://doi.org/10.1016/j.rse.2020.112275>, 2021.

739 Byrne, B., Liu, J., and Bowman, K. W.: Carbon emissions from the 2023 Canadian wildfires,
740 *Nature*, 633, 835–839, <https://doi.org/10.1038/s41586-024-07878-z>, 2024.

- 741 Chan, C. Y., Chan, L. Y., Harris, J. M., Oltmans, S. J., Blake, D. R., Qin, Y., Zheng, Y. G., and
742 Zheng, X. D.: Characteristic of ~~biomass-burning~~~~biomass-burning~~ emission sources, transport, and
743 chemical speciation in enhanced springtime tropospheric ozone profile over Hong Kong, J.
744 Geophys. Res., 108, 4015, <https://doi.org/10.1029/2001JD001555>, 2003.
- 745 Chang, J. H.-W., Wong, Y. J., Ooi, M. C.-G., Babu, S. R., Pani, S. K., and Lin, N.-H.: ~~Biomass~~
746 ~~burning~~~~Biomass-burning~~ in critical fire region over the Maritime Continent from 2012 to 2021: A
747 review of the meteorological influence and cloud-aerosol-radiation interactions, Atmos. Environ.,
748 320, 120324, <https://doi.org/10.1016/j.atmosenv.2023.120324>, 2024.
- 749 Chuang, M.-T., Lee, C.-T., Chou, C. C.-K., Lin, N.-H., Sheu, G.-R., Wang, J.-L., Chang, S.-C., Wang,
750 S.-H., Chi, K. H., Young, C.-Y., Huang, H., Chen, H.-W., Weng, G.-H., Lai, S.-Y., Hsu, S.-P., Chang,
751 Y.-J., Chang, J.-H., and Wu, X.-C.: Carbonaceous aerosols in the air masses transported from
752 Indochina to Taiwan: Longterm observation at Mt. Lulin, Atmos. Environ., 89, 507–516,
753 <https://doi.org/10.1016/j.atmosenv.2013.11.066>, 2014.
- 754 Cohen, J. B.: Quantifying the occurrence and magnitude of the Southeast Asian fire climatology,
755 Environ. Res. Lett., 9, 114018, <https://doi.org/10.1088/1748-9326/9/11/114018>, 2014.
- 756 Cohen, J. B., Lecoecur, E., and Hui Loong Ng, D.: Decadal-scale relationship between
757 measurements of aerosols, land-use change, and fire over Southeast Asia, Atmos. Chem. Phys.,
758 17, 721–743, <https://doi.org/10.5194/acp-17-721-2017>, 2017.
- 759
- 760 Cordero, R. R., Feron, S., Damiani, A., Carrasco, J., Karas, C., Wang, C., Kraamwinkel, C. T., and
761 Beaulieu, A.: Extreme fire weather in Chile driven by climate change and El Niño–Southern
762 Oscillation (ENSO), Sci. Rep., 14, 1974, <https://doi.org/10.1038/s41598-024-52481-x>, 2024.
- 763 Cui, D., Wang, J., Tan, L., and Dong, Z.: Impact of atmospheric wet deposition on phytoplankton
764 community structure in the South China Sea. Estuar. Coast. Shelf Sci. 173: 1–8,
765 <https://doi.org/10.1016/j.ecss.2016.02.011>, 2016.
- 766 Crutzen, P. J. and Andreae, M. O.: ~~Biomass Burning~~~~Biomass-burning~~ in the Tropics: Impact on
767 Atmospheric Chemistry and Biogeochemical Cycles, Science, 250, 1669–1678,
768 <https://doi.org/10.1126/science.250.4988.1669>, 1990.
- 769 Deeter, M. N., Edwards, D. P., Francis, G. L., Gille, J. C., Mao, D., Martínez-Alonso, S., Worden,
770 H. M., Ziskin, D., and Andreae, M. O.: Radiance-based retrieval bias mitigation for the MOPITT
771 instrument: the version 8 product, Atmos. Meas. Tech., 12, 4561–4580,
772 <https://doi.org/10.5194/amt-12-4561-2019>, 2019.
- 773 Dong, Z., Yang, R., Cao, J., Wang, L., and Cheng, J.: A strong high-temperature event in late-
774 spring 2023 in Yunnan province, Southwest China: Characteristics and possible causes. Atmos.
775 Res, 295, 107017. <https://doi.org/10.1016/j.atmosres.2023.107017>, 2023.

776 Espinoza, J.-C., Jimenez, J. C., Marengo, J. A., Schongart, J., Ronchail, J., Lavado-Casimiro, W.,
777 and Ribeiro, J. V. M.: The new record of drought and warmth in the Amazon in 2023 related to
778 regional and global climatic features, *Sci. Rep.*, 14, 8107, [https://doi.org/10.1038/s41598-024-](https://doi.org/10.1038/s41598-024-58782-5)
779 [58782-5](https://doi.org/10.1038/s41598-024-58782-5), 2024.

780 Fischer, E. M., Seneviratne, S. I., Vidale, P. L., Lüthi, D., and Schär, C.: Soil Moisture –
781 Atmosphere Interactions during the 2003 European Summer Heat Wave, *J. Climate*, 20, 5081–
782 5099, <https://doi.org/10.1175/JCLI4288.1>, 2007.

783 Forster, P., Storelvmo, T., Armour, K., Collins, W., Dufresne, J.-L., Frame, D., Lunt, D. J.,
784 Mauritsen, T., Palmer, M. D., Watanabe, M., Wild, M., and Zhang, H.: The Earth's Energy Budget,
785 Climate Feedbacks, and Climate Sensitivity, in: *Climate Change 2021: The Physical Science*
786 *Basis, Contribution of Working Group I to the Sixth Assessment Report of the Intergovernmental*
787 *Panel on Climate Change*, edited by: Masson-Delmotte, V., Zhai, P., Pirani, A., Connors, S. L.,
788 Péan, C., Berger, S., Caud, N., Chen, Y., Goldfarb, L., Gomis, M. I., Huang, M., Leitzell, K.,
789 Lonnoy, E., Matthews, J. B. R., Maycock, T. K., Waterfield, T., Yelekçi, O., Yu, R., and Zhou,
790 B., Cambridge University Press, Cambridge, United Kingdom and New York, NY, USA, pp. 923–
791 1054, <https://doi.org/10.1017/9781009157896.009>, 2021.

792 Forster, P. M., Smith, C., Walsh, T., Lamb, W. F., Lamboll, R., Hall, B., Hauser, M., Ribes, A.,
793 Rosen, D., Gillett, N. P., Palmer, M. D., Rogelj, J., von Schuckmann, K., Trewin, B., Allen, M.,
794 Andrew, R., Betts, R. A., Borger, A., Boyer, T., Broersma, J. A., Buontempo, C., Burgess, S.,
795 Cagnazzo, C., Cheng, L., Friedlingstein, P., Gettelman, A., Gütschow, J., Ishii, M., Jenkins, S.,
796 Lan, X., Morice, C., Mühle, J., Kadow, C., Kennedy, J., Killick, R. E., Krummel, P. B., Minx, J.
797 C., Myhre, G., Naik, V., Peters, G. P., Pirani, A., Pongratz, J., Schleussner, C.-F., Seneviratne, S.
798 I., Szopa, S., Thorne, P., Kovilakam, M. V. M., Majamäki, E., Jalkanen, J.-P., van Marle, M.,
799 Hoesly, R. M., Rohde, R., Schumacher, D., van der Werf, G., Vose, R., Zickfeld, K., Zhang, X.,
800 Masson-Delmotte, V., and Zhai, P.: Indicators of Global Climate Change 2023: annual update of
801 key indicators of the state of the climate system and human influence, *Earth Syst. Sci. Data*, 16,
802 2625–2658, <https://doi.org/10.5194/essd-16-2625-2024>, 2024.

803 Gelaro, R., McCarty, W., Suarez, M. J., Todling, R., Molod, A., Takacs, L., Randles, C. A.,
804 Darmenov, A., Bosilovich, M. G., Reichle, R., Wargan, K., Coy, L., Cullather, R., Draper, C.,
805 Akella, S., Buchard, V., Conaty, A., da Silva, A. M., Gu, W., Kim, G.-K., Koster, R., Lucchesi,
806 R., Merkova, D., Nielsen, J. E., Partyka, G., Pawson, S., Putman, W., Rienecker, M., Schubert, S.
807 D., Sienkiewicz, M., and Zhao, B.: The Modern-Era Retrospective Analysis for Research and
808 Applications, Version 2 (MERRA-2), *J. Climate*, 30, 5419–5454, [https://doi.org/10.1175/JCLI-D-](https://doi.org/10.1175/JCLI-D-16-0758.1)
809 [16-0758.1](https://doi.org/10.1175/JCLI-D-16-0758.1), 2017.

810 Giglio, L., Csizsar, I., and Justice, C. O.: Global distribution and seasonality of active fires as
811 observed with the Terra and Aqua Moderate Resolution Imaging Spectroradiometer (MODIS)
812 sensors, *J. Geophys. Res.-Biogeophys.*, 111, <https://doi.org/10.1029/2005JG000142>, 2006.

813 Giglio, L., Schroeder, W., and Justice, C. O.: The collection 6 MODIS active fire detection
814 algorithm and fire products, *Remote Sens. Environ.*, 178, 31–41,
815 <https://doi.org/10.1016/j.rse.2016.02.054>, 2016.

- 816 Giglio, L., Boschetti, L., Roy, D. P., Humber, M. L., and Justice, C. O.: The Collection 6 MODIS
817 burned area mapping algorithm and product, *Remote Sens. Environ.*, 217, 72–85,
818 <https://doi.org/10.1016/j.rse.2018.08.005>, 2018.
- 819 Gill, A. E.: Some simple solutions for heat-induced tropical circulation. *Q. J. R. Meteorol. Soc.*
820 106, 447–462. <https://doi.org/10.1002/qj.49710644905>, 1980.
- 821 Giles, D. M., Sinyuk, A., Sorokin, M. G., Schafer, J. S., Smirnov, A., Slutsker, I., Eck, T. F.,
822 Holben, B. N., Lewis, J. R., Campbell, J. R., Welton, E. J., Korkin, S. V., and Lyapustin, A. I.:
823 Advancements in the Aerosol Robotic Network (AERONET) Version 3 database– automated near-
824 real-time quality control algorithm with improved cloud screening for Sun photometer aerosol op-
825 tical depth (AOD) measurements, *Atmos. Meas. Tech.*, 12, 169–209, [https://doi.org/10.5194/amt-](https://doi.org/10.5194/amt-12-169-2019)
826 12-169-2019, 2019.
- 827 Gui, Y., Wang, K., Jin, Z., Wang, H., Deng, H., Li, X., Tian, X., Wang, T., Chen, W., Wang, T.,
828 and Piao, S.: The decline in tropical land carbon sink drives high atmospheric CO₂ growth rate in
829 2023, *Natl. Sci. Rev.*, nwae365, <https://doi.org/10.1093/nsr/nwae365>, 2024.
- 830 Hirsch, E. and Koren, I.: Record-breaking aerosol levels explained by smoke injection into the
831 stratosphere, *Science*, 371, 1269–1274, <https://doi.org/10.1126/science.abe1415>, 2021.
- 832 Hu, Y., Yue, X., and Tian, C.: Climatic drivers of the Canadian wildfire episode in 2023,
833 *Atmospheric and Oceanic Science Letters*, 17, 100483,
834 <https://doi.org/10.1016/j.aosl.2024.100483>, 2024.
- 835 Huang, H.-Y., Wang, S.-H., Huang, W.-X., Lin, N.-H., Chuang, M.-T., da Silva, A. M., and Peng,
836 C.-M.: Influence of Synoptic-Dynamic Meteorology on the Long-Range Transport of Indochina
837 ~~Biomass Burning~~ Biomass-burning Aerosols, *J. Geophys. Res.-Atmos.*, 125, e2019JD031260,
838 <https://doi.org/10.1029/2019JD031260>, 2020.
- 839 Huang, H.-Y., Wang, S.-H., Lau, W.K.M., Wang, S.-Y.S., and da Silva, A.M.: Impact of regional
840 climate patterns on the ~~biomass-burning~~ biomass-burning emissions and transport over Peninsular
841 Southeast Asia, 2000–2019. *Atmos. Res.* 297, 107067.
842 <https://doi.org/10.1016/j.atmosres.2023.107067>, 2024.
- 843 IPCC: Climate Change 2021 – The Physical Science Basis: Working Group I Contribution to the
844 Sixth Assessment Report of the Intergovernmental Panel on Climate Change, Cambridge
845 University Press, Cambridge, <https://doi.org/10.1017/9781009157896>, 2023.
- 846 Jain, P., Barber, Q. E., Taylor, S. W., Whitman, E., Castellanos Acuna, D., Boulanger, Y.,
847 Chavardès, R. D., Chen, J., Englefield, P., Flannigan, M., Girardin, M. P., Hanes, C. C., Little, J.,
848 Morrison, K., Skakun, R. S., Thompson, D. K., Wang, X., and Parisien, M.-A.: Drivers and
849 impacts of the record-breaking 2023 wildfire season in Canada, *Nature Communications*, 15, 6764,
850 <https://doi.org/10.1038/s41467-024-51154-7>, 2024.

851 Jones, M. W., Kelley, D. I., Burton, C. A., Di Giuseppe, F., Barbosa, M. L. F., Brambleby, E.,
852 Hartley, A. J., Lombardi, A., Mataveli, G., McNorton, J. R., Spuler, F. R., Wessel, J. B.,
853 Abatzoglou, J. T., Anderson, L. O., Andela, N., Archibald, S., Armenteras, D., Burke, E.,
854 Carmenta, R., Chuvieco, E., Clarke, H., Doerr, S. H., Fernandes, P. M., Giglio, L., Hamilton, D.
855 S., Hantson, S., Harris, S., Jain, P., Kolden, C. A., Kurvits, T., Lampe, S., Meier, S., New, S.,
856 Parrington, M., Perron, M. M. G., Qu, Y., Ribeiro, N. S., Saharjo, B. H., San-Miguel-Ayanz, J.,
857 Shuman, J. K., Tanpipat, V., van der Werf, G. R., Veraverbeke, S., and Xanthopoulos, G.: State
858 of Wildfires 2023–2024, *Earth Syst. Sci. Data*, 16, 3601–3685, [https://doi.org/10.5194/essd-16-](https://doi.org/10.5194/essd-16-3601-2024)
859 3601-2024, 2024.

860 Ke, P., Ciais, P., Sitch, S., Li, W., Bastos, A., Liu, Z., Xu, Y., Gui, X., Bian, J., Goll, D. S., Xi, Y.,
861 Li, W., O'Sullivan, M., Goncalves De Souza, J., Friedlingstein, P., and Chevallier, F.: Low latency
862 carbon budget analysis reveals a large decline of the land carbon sink in 2023, *National Science*
863 *Review*, 11, nwae367, <https://doi.org/10.1093/nsr/nwae367>, 2024.

864 Kim, M.-H., Omar, A. H., Tackett, J. L., Vaughan, M. A., Winker, D. M., Trepte, C. R., Hu, Y.,
865 Liu, Z., Poole, L. R., Pitts, M. C., Kar, J., and Magill, B. E.: The CALIPSO version 4 automated
866 aerosol classification and lidar ratio selection algorithm, *Atmos. Meas. Tech.*, 11, 6107–6135,
867 <https://doi.org/10.5194/amt11-6107-2018>, 2018.

868 Kolden, C. A., Abatzoglou, J. T., Jones, M. W., and Jain, P.: Wildfires in 2023, *Nat. Rev. Earth*
869 *Environ.*, 5, 238–240, <https://doi.org/10.1038/s43017-024-00544-y>, 2024.

870 Lai, G. and Zhang Y.: Increased atmospheric aridity and reduced precipitation drive the 2023
871 extreme wildfire season in Canada. *Geophys. Res. Lett.*, 52, e2024GL114492.
872 <https://doi.org/10.1029/2024GL114492>, 2025.

873 Liao, Z. H., Ling, Z. H., Gao, M., Sun, J. R., Zhao, W., Ma, P. K., Quan, J. N., and Fan, S. J.:
874 Tropospheric Ozone Variability Over Hong Kong Based on Recent 20 years (2000–2019)
875 Ozonesonde Observation, *J. Geophys. Res.-Atmos.*, 126, <https://doi.org/10.1029/2020jd033054>,
876 2021.

877 Lemus-Canovas, M., Insua-Costa, D., Trigo, R. M., and Miralles, D. G.: Record-shattering 2023
878 Spring heatwave in western Mediterranean amplified by long-term drought, *npj Climate and*
879 *Atmospheric Science*, 7, 25, <https://doi.org/10.1038/s41612-024-00569-6>, 2024.

880 Lee, C.-T., Ram, S. S., Nguyen, D. L., Chou, C. C., Chang, S.-Y., Lin, N.-H., Chang, S.-C., Hsiao,
881 T.-C., Sheu, G.-R., and Ou-Yang, C.-F.: Aerosol chemical profile of near-source **biomass**
882 **burning** smoke in Sonla, Vietnam during 7-SEAS campaigns in 2012 and 2013,
883 *Aerosol Air Qual. Res.*, 16, 2603–2617, 2016.

884 Lin, N.-H., Tsay, S.-C., Maring, H. B., Yen, M.-C., Sheu, G.-R., Wang, S.-H., Chi, K. H., Chuang,
885 M.-T., Ou-Yang, C.-F., Fu, J. S., Reid, J. S., Lee, C.-T., Wang, L.-C., Wang, J.-L., Hsu, C. N.,
886 Sayer, A. M., Holben, B. N., Chu, Y.-C., Nguyen, X. A., Sopajaree, K., Chen, S.-J., Cheng, M.-
887 T., Tsuang, B.-J., Tsai, C.-J., Peng, C.-M., Schnell, R. C., Conway, T., Chang, C.-T., Lin, K.-S.,
888 Tsai, Y. I., Lee, W.-J., Chang, S.-C., Liu, J.-J., Chiang, W.-L., Huang, S.-J., Lin, T.-H., and Liu,

- 889 G.-R.: An overview of regional experiments on ~~biomass-burning~~~~biomass-burning~~ aerosols and
890 related pollutants in Southeast Asia: From BASE-ASIA and the Dongsha Experiment to 7-SEAS,
891 *Atmos. Environ.*, 78, 1–19, <https://doi.org/10.1016/j.atmosenv.2013.04.066>, 2013.
- 892 Lin, C.-Y., Hsu, H.-M., Lee, Y. H., Kuo, C. H., Sheng, Y.-F., and Chu, D. A.: A new transport
893 mechanism of ~~biomass-burning~~~~biomass-burning~~ from Indochina as identified by modeling studies,
894 *Atmos. Chem. Phys.*, 9, 7901–7911, <https://doi.org/10.5194/acp-9-7901-2009>, 2009.
- 895 Lin, C. C., Chen, W. N., Loftus, A. M., Lin, C. Y., Fu, Y. T., Peng, C. M., and Yen, M. C.:
896 Influences of the long-range transport of biomass-burning pollutants on surface air quality during
897 7-SEAS field campaigns, *Aerosol Air Qual. Res.*, 17, 2595–2607,
898 <https://doi.org/10.4209/aaqr.2017.08.0273>, 2017.
- 899 Li, J. Li X. and Ying T.: North Atlantic and the Barents Sea variability contribute to the 2023
900 extreme fire season in Canada. *Proc. Natl Acad. Sci. USA*, 121 (49).
901 <https://doi.org/10.1073/pnas.241424112>, 2024.
- 902 Liu, H., Jacob, D. J., Chan, L. Y., Oltmans, S. J., Bey, I., Yantosca, R. M., Harris, J. M., Duncan,
903 B. N., and Martin, R. V.: Sources of tropospheric ozone along the Asian Pacific Rim: An analysis
904 of ozonesonde observations, *J. Geophys. Res.*, 107, ACH 3-1-ACH 3-19,
905 <https://doi.org/10.1029/2001JD002005>, 2002.
- 906 Liu, Z., Deng, Z., Davis, S. J., and Ciais, P.: Global carbon emissions in 2023, *Nature Reviews*
907 *Earth and Environment*, 1–2, <https://doi.org/10.1038/s43017-024-00532-2>, 2024.
- 908 [Liu, B., Fang, Y., Sun, S., Liu, L., and Cheah, W.: Extreme High Temperatures in the Indochina
909 Peninsula and Their Association With Enhanced Convection in the Horn of Africa and Arabian
910 Peninsula During Spring 2023. *Atmospheric Science Letters*. 27, no. 5: e70026.
911 <https://doi.org/10.1002/asl2.70026>, 2026.](https://doi.org/10.1002/asl2.70026)
- 912 Lyu, Y., Wang, J., Zhi, X., Wang, X., Zhang, H., Wen, Y., Park, E., Lee, J., Wan, X., Zhu, S.,
913 Dung, D.T.: The characterization, mechanism, predictability, and impacts of the unprecedented
914 2023 Southeast Asia heatwave. *npj Clim. Atmos. Sci.* 7, 246. <https://doi.org/10.1038/s41612-024-00797-w>, 2024.
- 916 Ma, T., Chen, W., Cai, Q., Dong, Z., Wang, L., Hu, P., Gao, L., Garfinkel, C.: Attribution analysis
917 of the persistent and extreme drought in Southwest China during 2022–2023. *Environ. Res. Lett.*
918 <https://doi.org/10.1088/1748-9326/ad8171>, 2024.
- 919 MacCarthy, J., Tyukavina, A., Weisse, M.J., Harris, N., & Glen, E., Extreme wildfires in Canada
920 and their contribution to global loss in tree cover and carbon emissions in 2023. *Global Change*
921 *Biology*, 30, e17392. doi:10.1111/gcb.17392, 2024.
- 922 McMillan, W. W., Barnet, C., Strow, L., Chahine, M. T., McCourt, M. L., Warner, J. X., Novelli,
923 P. C., Korontzi, S., Maddy, E. S., and Datta, S.: Daily global maps of carbon monoxide from

- 924 NASA's Atmospheric Infrared Sounder, *Geophys. Res. Lett.*, 32, L11801,
925 <https://doi.org/10.1029/2004GL021821>, 2005.
- 926 McMillan, W. W., Evans, K. D., Barnet, C. D., Maddy, E. S., Sachse, G. W., and Diskin, G. S.:
927 Validating the AIRS Version 5 CO retrieval with DACOM in situ measurements during INTEX-
928 A and -B, *IEEE T. Geosci. Remote*, 49, 2802–2813, <https://doi.org/10.1109/TGRS.2011.2106505>,
929 2011.
- 930 Michailidis, K., Garane, K., Karagkiozidis, D., Peletidou, G., Voudouri, K.-A., Balis, D., and Bais,
931 A.: Extreme wildfires over northern Greece during summer 2023 – Part A: Effects on aerosol
932 optical properties and solar UV radiation, *Atmospheric Research*, 311, 107700,
933 <https://doi.org/10.1016/j.atmosres.2024.107700>, 2024.
- 934 Min, S. K.: Human influence can explain the widespread exceptional warmth in 2023. *Commun.*
935 *Earth Environ.* 5, 215 <https://doi.org/10.1038/s43247-024-01391-x>, 2024.
- 936 Omar, A. H., Winker, D. M., Vaughan, M. A., Hu, Y., Trepte, C. R., Ferrare, R. A., Lee, K.-P.,
937 Hostetler, C. A., Kittaka, C., Rogers, R. R., Kuehn, R. E., and Liu, Z.: The CALIPSO automated
938 aerosol classification and lidar ratio selection algorithm, *J. Atmos. Ocean. Tech.*, 26, 1994–2014,
939 <https://doi.org/10.1175/2009JTECHA1231.1>, 2009.
- 940 Ou-Yang, C. F., Lin, N. H., Sheu, G. R., Lee, C. T., and Wang, J. L.: Seasonal and diurnal
941 variations of ozone at a high-altitude mountain baseline station in East Asia, *Atmos. Environ.*, 46,
942 279–288, <https://doi.org/10.1016/j.atmosenv.2011.09.060>, 2012.
- 943 Ou-Yang, C. F., Lin, N. H., Lin, C. C., Wang, S. H., Sheu, G. R., Lee, C. Te, Schnell, R. C., Lang,
944 P. M., Kawasato, T., and Wang, J. L.: Characteristics of atmospheric carbon monoxide at a high-
945 mountain background station in East Asia, *Atmos. Environ.*, 89, 613–622,
946 <https://doi.org/10.1016/j.atmosenv.2014.02.060>, 2014.
- 947 Ou-Yang, C. F., Ravindra Babu, S., Lee, J.-R., Yen, M.-C., Griffith, S. M., Lin, C.-C., Chang, S.-
948 C., and Lin, N.-H.: Detection of stratospheric intrusion events and their role in ozone enhancement
949 at a mountain background site in sub-tropical East Asia, *Atmos. Environ.*, 268, 118779,
950 <https://doi.org/10.1016/j.atmosenv.2021.118779>, 2022.
- 951 Pani, S. K., Wang, S. H., Lin, N. H., Lee, C. Te, Tsay, S. C., Holben, B. N., Janjai, S., Hsiao, T.
952 C., Chuang, M. T., and Chantara, S.: Radiative effect of springtime biomass-burning aerosols over
953 northern Indochina during 7-SEAS/BASELInE 2013 campaign, *Aerosol Air Qual. Res.*, 16, 2802–
954 2817, <https://doi.org/10.4209/aaqr.2016.03.0130>, 2016.
- 955 Pani, S. K., Ou-Yang, C.-F., Wang, S.-H., Ogren, J. A., Sheridan, P. J., Sheu, G.-R., and Lin, N.-
956 H. J. A. E.: Relationship between long-range transported atmospheric black carbon and carbon
957 monoxide at a high-altitude background station in East Asia, *Atmos. Environ.*, 210, 86–99,
958 <https://doi.org/10.1016/j.atmosenv.2019.04.053>, 2019.

- 959 Pani, S.K., Huang, H.-Y., Wang, S.-H., Holben, B.N., Lin, N.-H.: Long-term observation of
960 columnar aerosol optical properties over the remote South China Sea. *Sci. Total Environ.* 905,
961 167113 <https://doi.org/10.1016/j.scitotenv.2023.167113>, 2023.
- 962 Platnick, S., King, M. and Hubanks, P.: MODIS Atmosphere L3 Monthly Product.
963 https://doi.org/10.5067/MODIS/MOD08_M3.006, 2015.
- 964 Perkins-Kirkpatrick, S., Barriopedro, D., Jha, R., Wang, L., Mondal, A., Libonati, R., and
965 Kornhuber, K.: Extreme terrestrial heat in 2023, *Nature Reviews Earth & Environment*, 5, 244–
966 246, <https://doi.org/10.1038/s43017-024-00536-y>, 2024.
- 967 Raghuraman, S. P., Soden, B., Clement, A., Vecchi, G., Menemenlis, S., and Yang, W.: The 2023
968 global warming spike was driven by the El Niño–Southern Oscillation, *Atmos. Chem. Phys.*, 24,
969 11275–11283, <https://doi.org/10.5194/acp-24-11275-2024>, 2024.
- 970 Ramanathan, V., Crutzen, P. J., Kiehl, J. T., and Rosenfeld, D.: Aerosols, climate, and the
971 hydrological cycle, *Science*, 294, 2119–2124, <https://doi.org/10.1126/science.1064034>, 2001.
- 972 Ravindra Babu, S., Ou-Yang, C.-F., Griffith, S. M., Pani, S. K., Kong, S. S.-K., and Lin, N.-H.:
973 Transport pathways of carbon monoxide from Indonesian fire pollution to a subtropical high-
974 altitude mountain site in the western North Pacific, *Atmos. Chem. Phys.*, 23, 4727–4740,
975 <https://doi.org/10.5194/acp-23-4727-2023>, 2023.
- 976 Ravindra Babu, S. and Lin, N.-H.: Changing pattern of springtime ~~biomass burning~~
977 ~~burning~~ over Peninsular Southeast Asia (PSEA) in recent decades. *ESS Open Archive* . August
978 08, 2023. DOI: 10.22541/essoar.169111389.92212046/v2, 2023.
- 979 Reid, J. S., Hyer, E. J., Johnson, R., Holben, B. N., Yokelson, R. J., Zhang, J., Campbell, J. R.,
980 Christopher, S. A., Di Girolamo, L., Giglio, L., Holz, R. E., Kearney, C., Miettinen, J., Reid, E.
981 A., Turk, F. J., Wang, J., Xian, P., Zhao, G., Balasubramanian, R., Chew, B. N., Janai, S., Lagrosas,
982 N., Lestari, P., Lin, N.-H., Mahmud, M., Nguyen, A. X., Norris, B., Oahn, N. T. K., Oo, M.,
983 Salinas, S. V., Welton, E. J., Liew, S. C.: Observing and understanding the Southeast Asian aerosol
984 system by remote sensing: An initial review and analysis for the Seven Southeast Asian Studies
985 (7SEAS) program, *Atmos. Res.*, 122, 403–468, <https://doi.org/10.1016/j.atmosres.2012.06.005>,
986 2013.
- 987 Roy, D. P., De Lemos, H., Huang, H., Giglio, L., Houborg, R. and Miura, T.: Multi-resolution
988 monitoring of the 2023 Maui wildfires, implications and needs for satellite-based wildfire disaster
989 monitoring. *Sci. Remote Sens.* 10, 100142. <https://doi.org/10.1016/j.srs.2024.100142>, 2024.
- 990 Sayer, A. M., Munchak, L. A., Hsu, N. C., Levy, R. C., Bettenhausen, C., and Jeong, M. J.:
991 MODIS collection 6 aerosol products: comparison between Aqua's e-Deep Blue, Dark Target, and
992 “merged” datasets, and usage recommendations, *J. Geophys. Res. Atmos.*, 119, 13965–13989,
993 2014.

- 994 Seneviratne, S. I., Zhang, X., Adnan, M., Badi, W., Dereczynski, C., Di Luca, A., Ghosh, S.,
995 Iskandar, I., Kossin, J., Lewis, S., Otto, F., Pinto, I., Satoh, M., Vicente-Serrano, S. M., Wehner,
996 M., and Zhou, B.: Weather and Climate Extreme Events in a Changing Climate. In Proc. *Climate*
997 *Change 2021: The Physical Science Basis*. Contribution of Working Group I to the Sixth
998 Assessment Report of the Intergovernmental Panel on Climate Change, 1513–1766 (Cambridge
999 University Press, 2021). <https://doi.org/10.1017/9781009157896.013>, 2021
- 1000 Sheu, G.-R., Lin, N.-H., Wang, J.-L., Lee, C.-T., Ou Yang, C.-F., and Wang, S.-H.: Temporal
1001 distribution and potential sources of atmospheric mercury measured at a high-elevation
1002 background station in Taiwan, *Atmos. Environ.*, 44, 2393–2400,
1003 <https://doi.org/10.1016/j.atmosenv.2010.04.009>, 2010.
- 1004 Sinyuk, A., Holben, B. N., Eck, T. F., Giles, D. M., Slutsker, I., Korkin, S., Schafer, J. S., Smirnov,
1005 A., Sorokin, M., and Lyapustin, A.: The AERONET Version 3 aerosol retrieval algorithm,
1006 associated uncertainties and comparisons to Version 2, *Atmos. Meas. Tech.*, 13, 3375–3411,
1007 <https://doi.org/10.5194/amt-13-3375-2020>, 2020.
- 1008 Torbenson, M. and Büntgen, U.: summer warmth unparalleled over the past 2,000 years. *Nature*
1009 631, 94–97 (2024). <https://doi.org/10.1038/s41586-024-07512-y>, 2023.
- 1010 Tsay, S. C., Maring, H. B., Lin, N. H., Buntoung, S., Chantara, S., Chuang, H. C., Gabriel, P. M.,
1011 Goodloe, C. S., Holben, B. N., Hsiao, T. C., Christina Hsu, N., Janjai, S., Lau, W. K. M., Lee, C.
1012 Te, Lee, J., Loftus, A. M., Nguyen, A. X., Nguyen, C. M., Pani, S. K., Pantina, P., Sayer, A. M.,
1013 Tao, W. K., Wang, S. H., Welton, E. J., Wiriya, W., and Yen, M. C.: Satellitesurface perspectives
1014 of air quality and aerosol-cloud effects on the environment: An overview of 7-SEAS/BASELInE,
1015 *Aerosol Air Qual. Res.*, 16, 2581–2602, <https://doi.org/10.4209/aaqr.2016.08.0350>, 2016.
- 1016 Twomey, S.: The Influence of Pollution on the Shortwave Albedo of Clouds, *Journal of*
1017 *Atmospheric Sciences*, 34, 1149–1152, [https://doi.org/10.1175/1520-](https://doi.org/10.1175/1520-0469(1977)034<1149:TIOPOP>2.0.CO;2)
1018 [0469\(1977\)034<1149:TIOPOP>2.0.CO;2](https://doi.org/10.1175/1520-0469(1977)034<1149:TIOPOP>2.0.CO;2), 1977.
- 1019 [Vadrevu, K. P., Lasko, K., Giglio, L., Schroeder, W., Biswas, S., and Justice, C.: Trends in](https://doi.org/10.1038/s41598-019-43940-x)
1020 [Vegetation fires in South and Southeast Asian Countries, *Sci. Rep.*, 9, 7422,](https://doi.org/10.1038/s41598-019-43940-x)
1021 <https://doi.org/10.1038/s41598-019-43940-x>, 2019.
- 1022 Wang, S., Guan, L., Cohen, J.B., and Qin, K.: Reconstructing top-down global black carbon
1023 emissions using remote sensing and models, *Atmospheric Pollution Research*, 16, 10, (102633).
1024 <https://doi.org/10.1016/j.apr.2025.102633>, 2025.
- 1025 Wang, S., Cohen, J. B., Deng, W., Qin, K., and Guo, J.: Using a New Top-Down Constrained
1026 Emissions Inventory to Attribute the Previously Unknown Source of Extreme Aerosol Loadings
1027 Observed Annually in the Monsoon Asia Free Troposphere, *Earths Fut.*, 9, e2021EF002167,
1028 <https://doi.org/10.1029/2021EF002167>, 2021.

- 1029 Wang, S., Cohen, J. B., Guan, L., Lu, L., Tiwari, P., & Qin, K.: Observationally constrained global
1030 NO_x and CO emissions variability reveals sources which contribute significantly to CO₂
1031 emissions, *npj Climate and Atmospheric Science*, 10.1038/s41612-025-00977-2, 8, 1, 2025.
- 1032 Warner, J. X., Comer, M. M., Barnet, C. D., McMillan, W. W., Wolf, W., Maddy, E., and Sachse,
1033 G.: A Comparison of Satellite Tropospheric Carbon Monoxide Measurements from AIRS and
1034 MOPITT During INTEX-A, *J. Geophys. Res.*, 112, D12S17,
1035 <https://doi.org/10.1029/2006JD007925>, 2007.
- 1036 Warner, J., Carminati, F., Wei, Z., Lahoz, W., and Attié, J.-L.: Tropospheric carbon monoxide
1037 variability from AIRS under clear and cloudy conditions, *Atmos. Chem. Phys.*, 13, 12469–12479,
1038 <https://doi.org/10.5194/acp-13-12469-2013>, 2013.
- 1039 Wai, K. M., Lin, N., Wang, S., and Dokiya, Y.: Rainwater chemistry at a high-altitude station, Mt.
1040 Lulin, Taiwan: Comparison with a background station, Mt. Fuji, *J. Geophys. Res.-Atmos.*, 113,
1041 D06305, <https://doi.org/10.1029/2006JD008248>, 2008.
- 1042 Wei, J., Li, Z., Peng, Y., and Sun, L.: MODIS Collection 6.1 aerosol optical depth products over
1043 land and ocean: validation and comparison, *Atmos. Environ.*, 201, 428–440, 2019a.
- 1044 Wei, J., Li, Z., Sun, L., Peng, Y., and Wang, L.: Improved merge schemes for MODIS Collection
1045 6.1 Dark Target and Deep Blue combined aerosol products, *Atmos. Environ.*, 202, 315–327,
1046 2019b.
- 1047 Worden, H., Deeter, M., Edwards, D., Gille, J., Drummond, J., and Nédélec, P.: Observations of
1048 near-surface carbon monoxide from space using MOPITT multispectral retrievals, *J. Geophys.*
1049 *Res.-Atmos.*, 115, D18314, <https://doi.org/10.1029/2010JD014242>, 2010.
- 1050 Xia, L., Liu, R., Fan, W., and Ren, C.: Emerging carbon dioxide hotspots in East Asia identified
1051 by a top-down inventory, *Commun. Earth Environ.*, 6, 1–13, [https://doi.org/10.1038/s43247-024-](https://doi.org/10.1038/s43247-024-01991-7)
1052 [01991-7](https://doi.org/10.1038/s43247-024-01991-7), 2025.
- 1053 Yadav, I. C., Linthoingambi Devi, N., Li, J., Syed, J. H., Zhang, G., and Watanabe, H.: **Biomass**
1054 **burning** ~~Biomass-burning~~ in Indo-China peninsula and its impacts on regional air quality and global
1055 climate change – a review, *Environ. Pollut.*, 227, 414–427,
1056 <https://doi.org/10.1016/j.envpol.2017.04.085>, 2017.
- 1057 Zachariah, M., Vautard, R., Chaithra, S. T., Kimutai, J., Arulalan, T., AchutaRao, K., Otto, F. E.
1058 L.: Extreme humid heat in South and Southeast Asia in April 2023, largely driven by climate
1059 change, detrimental to vulnerable and disadvantaged communities. *World Weather Attribution*.
1060 <https://doi.org/10.25561/104092>, 2023.
- 1061 ~~Zeng, Z. and Sun, J.: Impacts of a tripolar sea surface temperature pattern over tropical North~~
1062 ~~Pacific on interannual variations of spring extreme consecutive dry days over southern China. *J.*~~
1063 ~~*Geophys. Res. Atmos.* 127, e2021JD036281. <https://doi.org/10.1029/2021JD036281>, 2022.~~
- 1064

